Optimization and extraction of functional information from *in vitro* flow models using dual-beam spectral-domain optical coherence tomography cross-correlation analysis

Susan M. Daly
Christophe Silien
Martin J. Leahy

Optimization and extraction of functional information from *in vitro* flow models using dual-beam spectral-domain optical coherence tomography cross-correlation analysis

Susan M. Daly,[a] **Christophe Silien,**[a,b] **and Martin J. Leahy**[c]
[a]University of Limerick, Department of Physics & Energy, Ireland
[b]University of Limerick, Materials and Surface Science Institute, Ireland
[c]National University of Ireland, School of Physics, Tissue Optics and Microcirculation Imaging Group, Galway, Ireland

Abstract. As *in vivo* flow behavior can be pulsatile, intermittent, and/or otherwise changeable with time, the ability to provide clinicians with a means of real-time visualization and functional assessment of structures is of particular importance. The discernment of pulsatile flow behavior using a dual-beam spectral domain optical coherence tomography system (db-SdOCT) by quasi-simultaneous measurement by two planes of illumination is demonstrated. By cross-correlation analysis, it is possible to compute velocity metrics pertaining to flowing particle motion, without *a priori* angular knowledge. This is the first application of cross-correlation-based dynamic assessment for the extraction of pulsatile behavior in an *in vitro* environment using an optimized db-SdOCT system. The experimental results outlined have shown the db-SdOCT system and its associated algorithms to be successful in the discernment of intermittent pulsatile flow behavior in *in vitro* models, concurrent to yielding velocity values in good agreement with that of the applied flow rate. © *2013 Society of Photo-Optical Instrumentation Engineers (SPIE)* [DOI: 10.1117/1.JBO.18.10.106003]

1 Introduction

Optical coherence tomography (OCT) has established itself a firm foothold in the realm of noninvasive optical medical diagnostic imaging, enabling *in vivo* cross-sectional tomographic visualization of the internal microstructure of biological systems, and is now considered an optical analogue to CT or magnetic resonance imaging, but with microscopic resolution. The original concept of OCT was to enable noninvasive real-time *in situ* imaging of tissue microstructure with a resolution approaching that of histology, but without the need for tissue excision and processing, i.e., an optical biopsy. The delay and magnitude of backscattered or remitted light detected by an OCT system carries information pertaining to the axial structure of semitransparent objects. OCT has a ubiquitous presence, having emerged in a variety of clinical fields: ophthalmology,[1,2] intravascular imaging in cardiology,[3,4] oncology,[5,6] gastroenterology,[7–9] general dermatology,[10,11] dentistry,[12,13] and gynecology,[14,15] to name a few. Fundamentally, OCT is an important clinical asset as it can be used to separate three-dimensional (3-D) structural and functional information in individual microvessels.

Doppler ultrasound, the underlying principle upon which Doppler OCT (DOCT) is based, was developed as a tool for vascular disease assessment and monitoring. However, despite the advancements of DOCT techniques, a principal limitation still exists: the Doppler method is inherently one-dimensional (1-D). The use of the Doppler functionality has been the predominant force for the quantification of moving particles within media. However, Doppler phase shift assessment of velocity values requires that the angle between the incident light source and the vessel in question be known *a priori*. The true velocity is extracted from this 1-D information by assuming the direction of blood motion, resulting in an inaccurate determination of the flow velocity.[16] It has been shown that Doppler techniques are apt only for larger blood vessels with faster flow rates, in which Doppler shifts are easier to detect.[17] Furthermore, as a Fourier transformation is usually performed by sliding short-time windows, tradeoffs between axial and velocity resolutions exist in the flow estimation.[18] DOCT is also inherently sensitive to the phase stability caused by both the system and the measurement environments.[19] In optical microangiography, (OMAG), spectral interferograms are modulated by a constant Doppler frequency (in hardware, e.g., by a piezo-translation stage, and in software), thereby making separation of the moving and static scattering components within the sample feasible. A further advancement of the OMAG modality came in the form of Doppler OMAG, a method which encompasses the advantages of both OMAG and the phase-resolved OCT methods.[20]

Speckle variance (SV) techniques based on structural image intensity have been used in tumor microvascular imaging with high-frequency ultrasound.[21] SV-OCT images accentuate blood vessels as flowing portions by analyzing localized speckle patterns that are uncorrelated between frames.[22] SV-OCT imaging has been reported in the dynamic monitoring of antivascular treatment effects (e.g., photodynamic therapy)[23] and in the analysis of the developing embryonic mammalian environment.[24] One of the most outward advantages of SV-OCT is its independence of the Doppler angle for flow velocity

Address all correspondence to: Susan M. Daly, University of Limerick, Department of Physics & Energy, Ireland. Tel: +353 61 204824; Fax: +353 61 202423; E-mail: susan.mcelligott@ul.ie

computations and its simplicity, with little additional computational complexity. In addition, as it is intrinsically based on contrast, SV techniques have a potential benefit over fluorescence microscopy, especially when the neovasculature exhibits increased permeability.[23] However, there are issues relating to the interpretation of the variance results obtained. The calculated variance is on the range of $\pm\infty$; and is dependent on the chosen window size. Thus, variance itself does not directly indicate flow and *a priori* structural knowledge is required to separate static and dynamic regions. In addition, SV-OCT suffers from multiple scattering-induced artifacts and interframe bulk tissue motion;[25,26] this can lead to spurious values of artificial contrast wrongly indicating the presence of vessels beneath real blood vessels.

A speckle pattern is formed either by the reflection of coherent light from a rough surface or by transmitting the light through a transparent medium having a randomly fluctuating refractive index distribution and by subsequent 3-D multiple beam interference.[27] The speckle pattern is a granular variation of light intensity obtained from any rough surface such as skin and is characterized by a random intensity distribution that may be described by statistical means.[28,29] Scattering inhomogeneities within the skin can be considered as point sources, and small differences in distances traversed result in dark and bright speckles dispersed at all points in space. This motion results in a speckle pattern that appears decorrelated or blurred.[30] The amount of decorrelation depends on the speed and volume of the scatterers in the tissue. Determinations of velocity may be obtained by temporally assessing the statistical behavior of speckles. Although specular reflection effects may be disregarded with the addition of polarizing filters, static tissue reduces the signal-to-noise ratio.[31–33] These factors contribute to the confinement of the speckle technique to superficial measurements, necessitating deeper measurements performed on surgically exposed tissue. Statistical information discernible from OCT data has been used for other purposes. For example, in fluorescence correlation spectroscopy (FCS), the mean-squared intensity fluctuation divided by the squared mean image intensity is equal to the reciprocal of the mean number of independent fluorescent particles per laser beam volume;[34] optical correlation methods are imaging analogues of FCS. Qualitatively and quantitatively, transient intensity changes have been used previously to discern various metrics concerning *in vitro* and *in vivo* environments.[35]

The study of the flow dynamics in blood vessels with complex geometry is important in rheology and cardiology to better understand the impact of localized blood flow. Resultantly, the advantageous aspects of noninvasive *in vivo* imaging modalities stem from their ability to provide clinically relevant information without disturbing the normal biological environment. This is borne out of recognition of the vitally important role that blood flow plays in the health of the individual.[36] The ability to provide a clinician with real-time visualization and guidance of an *in vivo* structure is particularly important for imaging purposes as flow can be pulsatile, intermittent, and/or otherwise changeable with time.[37] Enabling and adapting a method to discern such functional information expands the remit in which the method is useful. Although the ability to discern and quantify pulsatility allows characterization of such transient phenomena in its own right, it also permits its gating if it is hampering imaging applications through the introduction of temporal artifacts, e.g., in dynamic electrocardiogram-gated CT.[38]

As *in vivo* flow is generally pulsatile in nature, this imposes an added restriction for imaging modalities; i.e., the time over which the sequence of exposures is acquired must be small compared to the period of the pulse.[39] Blood flow dynamics such as pulsatility and autoregulation have been shown to change throughout the progression of ocular diseases such as diabetic retinopathy and glaucoma.[40] In addition, the administering of anesthesia can effect total blood flow;[41] e.g., isoflurane is a known vasodilator at high concentrations, and the monitoring of the effects of such are of clinical importance. Irregularities regarding known pulsatility behavior also provide valuable clinical knowledge; for example, pseudoaneurysms or false aneurysms are tender pulsatile arterial masses that can occur as a result of previous invasive medical intervention that necessitated intrusion into an artery,[42] e.g., stent placement. Correct characterization of such a pseudoaneurysm (which can be misinterpreted as an abscess) is vital, as incision or drainage could lead to extensive hemorrhage. Assessment of the effects on flow caused by vascular abnormalities, e.g., stenosis, can provide a direct overview of the stresses imposed on the plaque by the flow field and thus provide a means of estimating the likelihood of possible rupture. Investigations into related pulsatile waveform anomalies can provide such stress information, thereby enabling a prognosis of the associated dangers of particular stenotic lesions.[43]

There exist different means of extracting pulsing phenomena from *in vitro* and *in vivo* samples, as evident from the relevant literature. Aside from imaging methods, techniques that monitor physical changes due to blood flow have also been highly successful in characterizing transient processes. For example, pulsatile ocular blood flow assessment has been calculated from the ocular pulse wave produced by the bolus of blood entering the eye during cardiac systole. The volumetric blood changes caused by this imbalance are transferred to a pressure gradient that is recorded by a pneumotonometer.[44] In addition, ocular fundus pulsation can be assessed by measuring distance changes between cornea and retina during the cardiac cycle.[45]

Sequential images of selected vessels obtained by Doppler means allow correlation to the phases of the cardiac cycle obtained synchronously by a pulse plethysmograph.[46–48] Doppler ultrasound spectrum mode is a method of clinical importance as the spectral display is usually calculated at a particular location within a blood vessel using a short-time FFT method. The velocity (or Doppler frequency) distribution is illustrated as a function of time, making it especially useful for imaging pulsatile flow.[41] Methods utilizing the optical interferometric principle have been employed to investigate pulsatility: averaged Doppler shift, normalized velocity variance, and integrated phase difference all plotted over each instant in time, revealing a pulsing pattern.[49] In addition, the pulsatility of blood flow in a vessel can be observed through time-varying changes in phase variance, demonstrating the ability to study blood flow dynamics *in vivo*.[44,49,50] *En face* Doppler OCT methods have been utilized to measure pulsatile blood flow by gating methods[51] and by rapid repeated scanning of a small area to characterize pulsatility.[52] Phase analysis methods allow the assessment of murine coronary artery dynamics by utilizing cardiac cycle averaging and phase wrapping.[53]

Improving axial resolution values by one order of magnitude to the submicron region (and two orders of magnitude compared to conventional ultrasound), ultrahigh-resolution OCT has enabled the superior visualization of tissue microstructure,

e.g., cellular resolution imaging in opaque media. In order to improve axial resolution (Δz), the spectral bandwidth must be either increased or the central wavelength decreased; therefore, novel light sources are necessary.[54–56] The light source choice not only determines the axial resolution, but also influences both the penetration in the sample and the transverse resolution. Hence, the light source is the key technology and the appropriate choice of it is imperative. As the wavelength in a material of higher refractive index becomes shorter, the actual axial resolution may be determined by $\Delta z/\eta_G$, where the group refractive index η_G is typically 1.35 to 1.4 for most biological tissue. Nevertheless, the axial resolution is limited not only by the sample dispersion, but also by absorption and scattering within the sample.

Due to the extensive tortuosity of the microvasculature (especially if ailments that alter the physiology are present), the theoretical formulation of Doppler-based methods is dependent on knowledge of the angle involved, and resultantly, this may lead to over-/underestimations of velocities present or incomplete vascular maps *in vivo*. In an effort to surmount this restriction, the assessment of pulsatility in *in vitro* flow models by dual-beam cross-correlation spectral-domain optical coherence tomography (db-SdOCT) is described. db-SdOCT operates by quasi-simultaneous illumination and measurement of two distinct planes; the theoretical framework and a detailed outline of the associated algorithm are discussed in Ref. 57.

Analysis of temporally and spatially displaced light intensity fluctuations of light beams a known distance apart yields transit times that may be deduced via temporal cross-correlation, thereby yielding velocity values irrespective of vessel tortuosity. The db-SdOCT technique eliminates the need for angular information and utilizes the temporally evolving phase as a metric for quantifying velocity by statistical means. Presented here is the first application of such angle-independent correlation-based dynamic assessment for the extraction of pulsatile behavior, in addition to velocity values, in an *in vitro* environment. As a prelude to this work, optimization of the db-SdOCT methodology in terms of differing light source characteristics (λ_0, $\Delta\lambda$) is investigated.

2 Outline of db-SdOCT System: Light Source Optimization

The db-SdOCT system used in these studies was an in-house dual-beam design as depicted in Fig. 1. The light source primarily used was a superluminescent diode broadband source (Denselight, Singapore), with a center wavelength of 1310 nm and a spectral width (FWHM) of 130 nm (axial resolution, $\Delta z = 5.83~\mu m$). The system was split into two separate subsystems via fiber beam splitters (50/50 and 99/1 varieties; 99% of this was fed to the sample arms). Each sample arm had its own independent reference arm. The two sample arms were then coupled to a bulk optic beam splitter (50/50) and subsequently
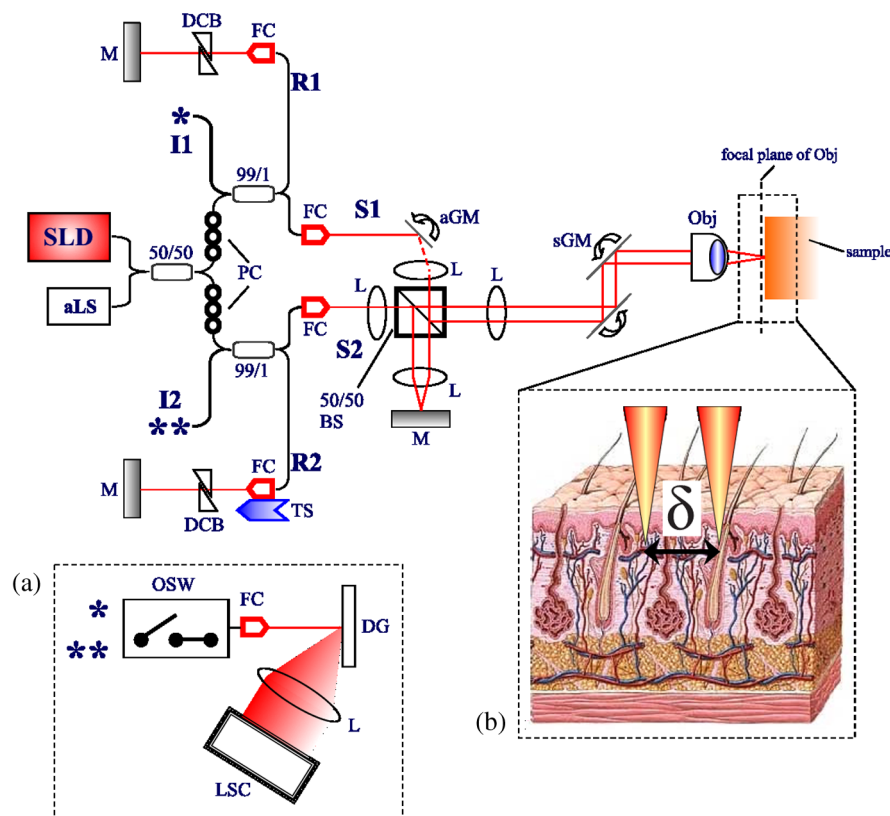

Fig. 1 Schematic diagram of the dual-beam spectral domain optical coherence tomography (db-SdOCT) system setup. SLD, superluminescent diode; aLS, HeNe alignment light source; M, dielectric broadband mirror; TS, manual translation stage; S, R, I, respective sample, reference, and interference arms; $x/(1-x)$, fiber optic beam splitter; 50/50 BS, bulk optic 50/50 beam splitter; PC, polarization controller; DCB, dispersion compensation block; FC, fiber coupler; L, achromatic lens; aGM, galvo mirror for angular control of sample beam separation; sGM, scanning galvo mirrors; Obj, objective lens. (a) Depiction of the optical switch (OSW) mechanism used to alternately present each sample arm signal to the diffraction grating (DG) of a spectrograph and for detection by a line scan CCD camera (LSC). (b) δ denotes the centroid separation of the sample beams, dictated by aGM movement. (Note: the converging and diverging of each sample arm beam at the focal plane is not shown for clarity.)

to a two-dimensional galvo arms system (sGM) for raster scanning through the system objective lens (LSM03, Thorlabs, Ltd., Ely, UK). As correlation analysis was already shown to provide reliable flow quantification,[57] the calibrated movement of a single galvo-scanning arm (aGM in Fig. 1) ensured precise control of the separation values, δ. An optical switch was employed as a means of discriminating the interferometric data of each channel for detection by a digital line scan camera (InGaAs, $f_{max} \cong$ 47 kHz; Goodrich, CA) and provided full-depth ranging for each channel. The camera was preceded by a spectrograph centered at 1310 nm (BaySpec, NJ). Automation of the system was implemented in LabVIEW, which controlled sequential system triggering, data acquisition, and data collection.

As can be seen from Fig. 1, only one camera and spectrograph is utilized in the system. In order to alternately present each channel's data for detection, it was necessary to apply an apt software trigger to the system (LabVIEW; National Instruments, UK) to initiate data acquisition, sequential data storage, and channel switching, ensuring no channel crosstalk/overlap, which would otherwise render unusable data. To do this, it was necessary to take into consideration the switching time between measurements. This switching time (τ) was deduced by

$$\tau = T_{OSWf} + t_A, \qquad (1)$$

where T_{OSWf} is the reciprocal of the optical switching frequency and t_A is the acquisition time. The transit time, t_t, is the theoretical time taken for a particle to pass through both planes of illumination of the db-SdOCT system a fixed distance apart (δ), at a particular velocity; this is $t_t = \delta/\bar{v}$. To provide flow to the capillaries, a syringe pump was used (PHD2000; Harvard Apparatus Ltd., Kent, UK). Applied flow rate values within capillaries were allowed 5-min settling time to avoid any unnecessary turbulent effects that may affect the resulting correlation computation.

2.1 Outline of Data Processing and Cross-Correlation Algorithm

Upon acquiring each image of ($y \times 1024$) pixels (where y is the number of vertical pixels per image), this was averaged along y to mitigate the effects of noise. All data were acquired via a technical data management streaming (TDMS) file in LabVIEW, a file type that is portable to other applications such as Excel. Due to the triggering of camera acquisition and data capture, each alternate column in the TDMS file contained information about either channel's structural (and therefore) functional information. All computational processing was performed using Matlab (R2007b, The Mathworks Inc.).

A univariate signal is a single observed variable that varies as a function of time or position. OCT data may be considered as a stochastic univariate time series with chronologically ordered observations at regular intervals.[58] An image time series recorded from detection channels A and B (ChA, ChB) may be considered to be a matrix of raw OCT intensity values stored as a function of pixel location (j) and of image number (n).

$$I_{A|B}(n) = OCT_{A|B}(j, n), \qquad (2)$$

where $OCT_{A|B}$ refers to the raw OCT data obtained for channels A and B of the db-SdOCT system; j ranges from ($1 : 1024$) pixels of the linear CCD; n ranges from ($1 : N$), N being the total

number of A-scans acquired. Due to the optical switching, the data were collected in alternating columns and as such were easily separated for correlation computation; all odd and even columns were grouped together as two individual datasets representing the OCT data acquired by both ChA and ChB. An equivalent representation of the previously defined discrete intensity matrix is as a function of image space and capture time for each channel of the dual-beam system.

$$I_{A[i+(i-1)]} = OCT_A(j, T/2) \qquad I_{B[2i]} = OCT_B(j, T/2), \qquad (3)$$

where i ranges from ($1 : N/2$); the total time for acquisition of both channels is $T = N \cdot \tau$. After spectral calibration of each side of the db-SdOCT system to optimize system sensitivity and signal quality,[59] a k-space interpolation and sequent FFT was applied. For these experiments, both amplitude and phase information were saved for further comparative analysis. The phase (θ) was deduced by the following:

$$\theta(j, n) = \tan^{-1}\left(\frac{Im[OCT_{A|B}(j, n)]}{Re[OCT_{A|B}(j, n)]}\right), \qquad (4)$$

where Im and Re indicate the imaginary and real components, respectively. The dynamic aspects of the intraluminal data of the *in vitro* models were considered, as outside of the lumen of the vessel, e.g., at the vessel walls, there (ideally) occurs no change in state with time, thereby rendering high correlation values irrespective of the flow within. The hemodynamic relevance of intraluminal measurements particularly in cardiovascular high-risk patients with type 2 diabetes has recently been reported.[60] The intraluminal column data of each channel was cross-correlated in time by means of the following expression:

$$C_{AB}(k) = \frac{\sum_{i=1}^{p}(I_{Ai} - \bar{I}_A)(I_{Bi} - \bar{I}_B)}{\sqrt{\sum_{i=1}^{p}(I_{Ai} - \bar{I}_A)^2 \sum_{i=1}^{p}(I_{Bi} - \bar{I}_B)^2}}\Bigg|_k, \qquad (5)$$

where C_{AB} refers to the relative correlation values obtained with between ChA and ChB; k is the range from ($1 : N/2$); p is the total number of intraluminal pixels chosen for correlation testing; $I_{A/B}$ implies the average of the intraluminal pixels considered. The resulting correlation values are of the range of (0 ± 1) indicating weak and strong correlation, respectively. As the flow rates applied generated laminar flow within the capillary (calculated as having Re < 1800, where Re is the Reynolds number), it was anticipated that for a specific flow rate, values of high correlation between both channels would occur at a certain point in time. As each correlation calculation represents a different point in time, it is expected that maximum correlation values between each channel converge at a later time for slower values of flow and vice versa. Consequently, temporal correlation maps[57] were computed (see Fig. 2), which illustrate relative correlation values with time providing a visual means of correlation assessment for different flow rates.

After computation of the correlation map, the temporal locations of correlation maxima were averaged for the intraluminal data considered, yielding the transit time, t_t, for flow passing between both illumination planes in succession. As for Doppler-related processing procedures in which the centroid of the power spectrum was taken as the Doppler frequency,[61] the mean of the transit time obtained for all A-scans using the cross-correlation method was used to compute velocity values. Last, division of
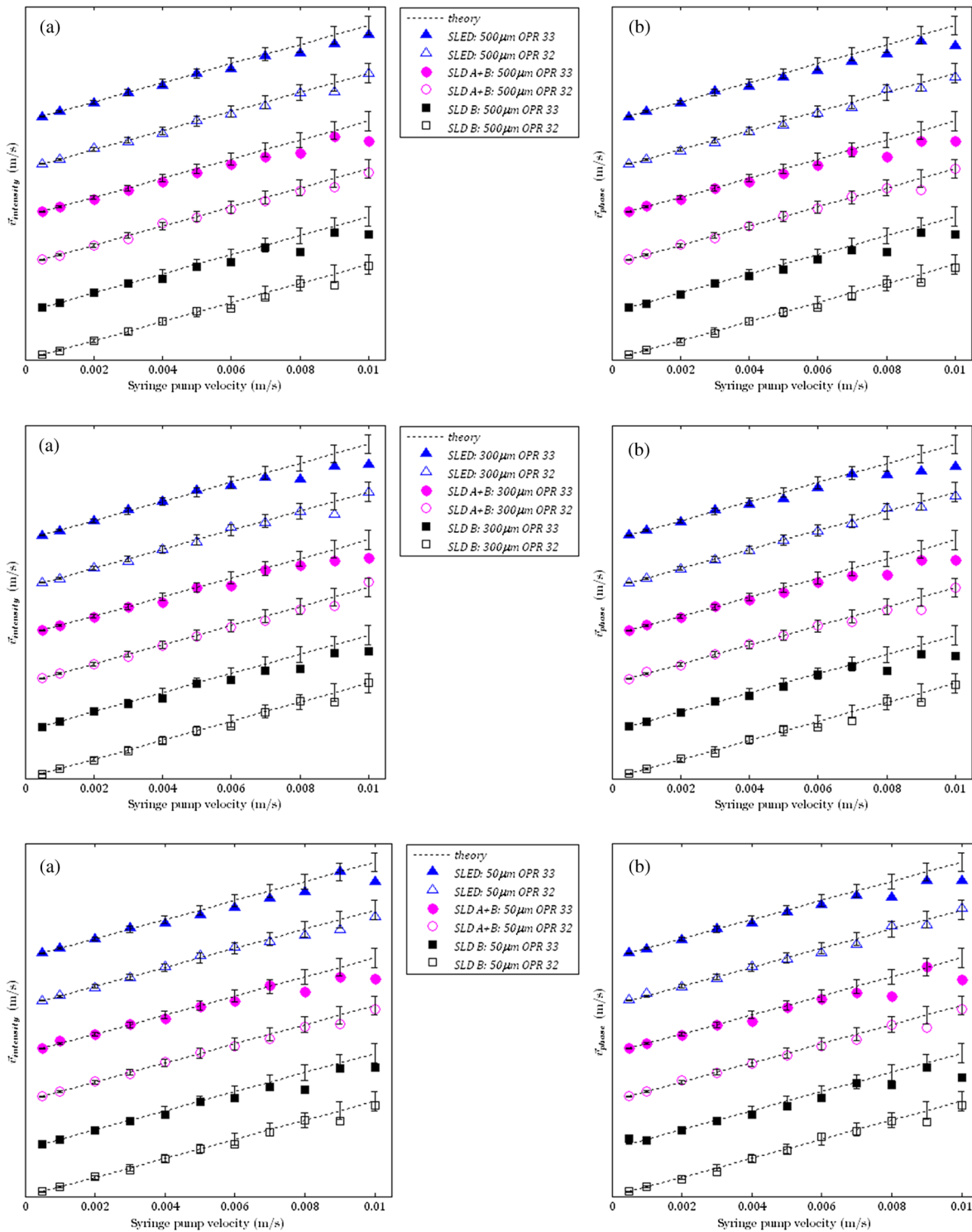
Fig. 2 Illustration of computational analysis flow chart of intraluminal capillary data. Cross-correlation analysis of each channel yields a temporal correlation map, from which regions of maximal correlation may be seen. Computation of the maximal correlation values between channels renders a time difference if multiplied by τ. Division of this into the predetermined value for the beam separation δ yields values for transverse velocity.

the relative separation distance δ by this value of t_t yields a value for the transverse velocity.

2.2 Impact of Coherence Focal Volume: Light Source Optimization

The means by which velocity data are obtained using the db-SdOCT algorithm and the associated optics are quite dissimilar

from the computational aspects of Doppler-related processing. As such, investigating the effects of a variety of light sources (with differing spectral characteristics) on the effectiveness of the cross-correlation algorithm is an instructive exercise, especially with a view to full system characterization and optimization.

Low-coherence light may be characterized as having statistical phase discontinuities over a distance known as the

coherence length, which is inversely proportional to the bandwidth of light. When such light is used, interference is only observed when the path lengths of the reference and sample arms are temporally/spatially matched to within the coherence time/length of the light. The coherence length (l_C) of light is defined as the spatial extent along the propagation direction over which the electric field is substantially correlated and is equal to the width of the field autocorrelation function.[62]

$$l_C = \frac{4 \ln(2)}{\pi} \frac{\lambda_0^2}{\Delta \lambda}, \tag{6}$$

where λ_0 is the source center wavelength and $\Delta\lambda$ is the FWHM bandwidth. The coherence length is related to the coherence time by $l_C = c\tau_C$, where c is the speed of light. Therefore, the axial resolution may be determined by the source coherence length (i.e., the arrival of time echoes), or more accurately, $\Delta z = (l_C/2)$. Although the above expression for l_C is for a Gaussian lineshape, it is the most common form used in OCT literature as it approximates the spectral shape of actual light sources and has useful Fourier transform properties.[63]

Utilizing ultra-broadband light sources in an OCT setup can provide much improved values of axial resolution; however, they are also prone to chromatic dispersion in optically dense materials such as glass, tissue, and water. As the speed of light is dependent on the refractive index [$\eta(k)$] of the material, certain spectral components are slowed down to a greater extent than others, hence causing dispersion. A dispersion mismatch can occur if different lengths of optical fiber or other dispersive media are present in the sample and reference arms. Considerable amounts of dispersion can be tolerated if the dispersion present in the interferometer arms is equal, thus creating a coherence function free from dispersion artifacts. If dispersion is present, the coherence function will not only broaden due to the dispersive imbalance but its peak intensity will decrease also, and therefore degrade the axial resolution and reduce sensitivity (dynamic range). A dispersion imbalance introduces a frequency-dependent phase shift $e^{i\theta(k)}$ in the complex spectral density as a function of the wave vector k, resulting in an FWHM increase in the corresponding interferogram. Material dispersion, $k(\omega) = [\eta(\omega)\omega/c]$, can be expanded into many different orders and is best described by a Taylor series expansion.[64]

$$k = \underbrace{k_0}_{*} + \underbrace{\frac{\partial k}{\partial \omega}(\omega - \omega_0)}_{\circ} + \underbrace{\frac{1}{2}\frac{\partial^2 k}{\partial \omega}(\omega - \omega_0)^2}_{} + \cdots$$
$$+ \frac{1}{n!}\frac{\partial^n k}{\partial \omega^n}(\omega - \omega_0)^n, \tag{7}$$

where $\omega = 2\pi v$. The first two terms are not related to dispersive broadening; * denotes zero-order dispersion and adds a constant offset; ∘ relates to first-order dispersion or group velocity, which changes the coherence length ($l_C' = \frac{l_C}{\eta_G}$), where η_G is the group index and can improve depth resolution as $\eta_G > 1$; and ⌣ indicates second-order dispersion (group velocity dispersion) and degrades depth resolution by a factor of $(1 - l\beta\Delta\lambda)^{0.5}$, where l is the length of the dispersive path and $\beta = (\mathrm{d}\eta_G/\mathrm{d}\lambda)$ is the group dispersion.[65] The impact of dispersion on the A-scan signal can be derived from the effect on the coherence function.

As previously discussed in Sec. 1, the light source not only determines the axial resolution, but also influences both the sample penetration and the transverse resolution. In this investigation, three different light sources were tested with varying values of probing coherent volume. In this investigation, three different light sources were tested with varying values of probing coherent volume: a relatively inexpensive superluminescent diode (SLED) broadband source (model DL-BX10; Denselight, Singapore) and two sources of an extended broadband SLD source (model LS2000B; Thorlabs, Ltd., Ely, UK). All relevant specifications for the light sources used are shown in Table 1. In the LS2000B, a multiplexed dual SLD arrangement of two fiber-pigtailed SLDs provides a single extended bandwidth ($\Delta\lambda = 200$ nm, typical) light source.

Given the aforementioned higher-order dispersive effects evident in ultra-broad bandwidth sources, the variation in longitudinal and transverse resolution values, and penetrative depth of field differences, the effects of these various characteristics are assessed individually using the db-SdOCT system and subsequent cross-correlation processing. Three different capillary sizes were investigated (500, 300, and 50 μm), at various flow rates of 2% intralipid solution (0.5 to 10 mm/s) and different acquisition rates of the line scan camera (OPR33 = 16,846 Hz; OPR32 = 31,680 Hz). To provide flow to the capillaries, a syringe pump was used (PHD2000; Harvard Apparatus Ltd.). Flow velocity values within capillary were allowed 5-min settling time to avoid any unnecessary turbulent effects that may affect the resulting velocity measurements. All light sources underwent a separate spectral calibration to yield the appropriate coefficients for equidistant sampling from λ-space to k-space for subsequent FFT processing. All data from each light source were cross-correlation processed in the same manner to yield velocity values and directionality data.

In terms of the acquisition rate used, OPR32 outperformed OPR33 with ~1.94 times increased accuracy at emulating the desired applied flow rates obtained by both intensity and phase-based analysis; see Fig. 3. As such, decreasing the db-SdOCT system acquisition rate negatively impacts on the results of computed values of velocity in terms of cross-correlation analysis. Longer exposure times (i.e., OPR33), although they permit an increased SNR, can result in motion-induced blurring, and

Table 1 Outline of the spectral characteristics of the various light sources used to investigate their effects in dual-beam spectral domain optical coherence tomography cross-correlation assessment.

			LS2000B	
		1310 nm SLED	SLD B	SLD A+B
m	λ_0	1.31E-06	1.34E-06	1.30E-06
m	$\Delta\lambda$	1.30E-07	1.10E-07	2.00E-07
—	$\eta_{\text{intalipid-glass}}$	1.35	1.35	1.35
μm	Δx	34.02	34.80	33.76
μm	l_C	8.63	10.67	5.52
μm^3	$V_{\text{coherence}}$	9985.98	12920.38	6294.95
mm	b	2.78	2.84	2.75

Note: Δx is the transverse resolution; $V_{\text{coherence}}$ is the probing coherent volume; b is the confocal parameter.

$$c_{AB}(k) = \frac{\sum_{i=1}^{p}(I_{Ai}-\overline{I_A})(I_{Bi}-\overline{I_B})}{\sqrt{\sum_{i=1}^{p}(I_{Ai}-\overline{I_A})^2 \sum_{i=1}^{p}(I_{Bi}-\overline{I_B})^2}}$$

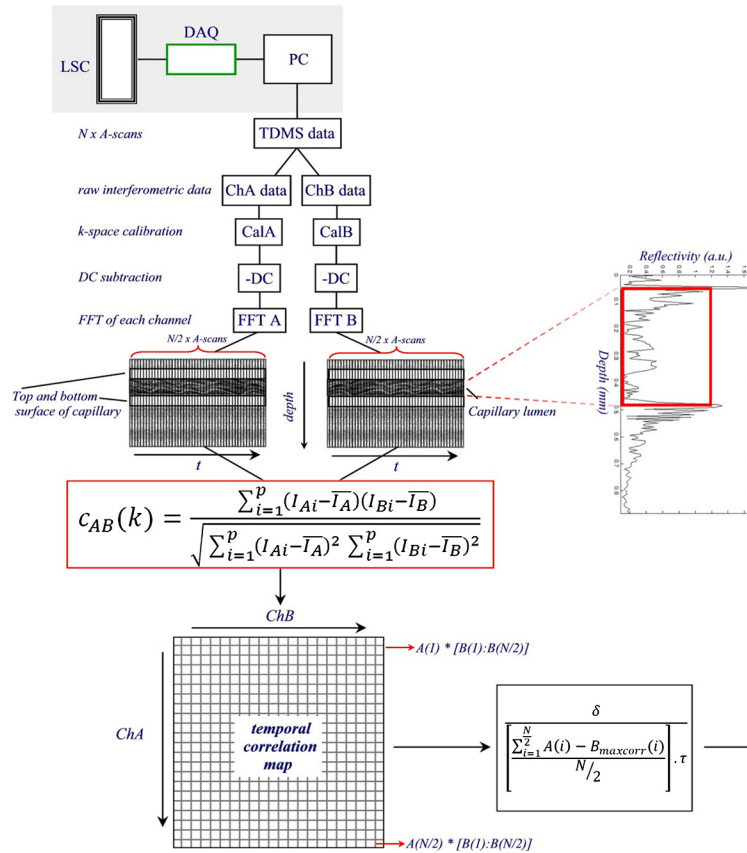$$\left[\frac{\sum_{i=1}^{\frac{N}{2}} A(i) - B_{maxcorr}(i)}{N/2}\right] \cdot \tau$$

Fig. 3 Graphical data showing velocity values obtained by (a) intensity and (b) phase correlation analysis. Three different light sources were considered and tested on three different capillary sizes, 500 μm (top), 300 μm (center), and 50 μm (bottom) and at two different acquisition speeds (OPR3 = 16,846 Hz; OPR32 = 31,680 Hz). Error bars: ±10% of values provided by syringe pump.

consequently, the information captured within that instant is not as distinct for correlation purposes at it would be if a higher acquisition rate (OPR32) was used. However, precisely how fast an exposure time can be implemented and successfully supply the user with adequate velocity data remains to be seen.

The deviation of velocities from their theoretically predicted values increased with decreasing capillary diameter; errors over all velocities and acquisition rates for capillary sizes 500, 300, and 50 μm were, respectively, 7.88, 7.92, and 8.41%. The primary purpose of this experiment was to investigate whether correlation-based results performed better with increased or decreased focal volume metrics. It was found that the deviation from theoretically anticipated velocities for averaged values of all phase- and intensity-based velocity data and all capillary sizes tested varied as follows (errors in parentheses): 1310 nm SLED (7.77%), 1340 nm SLD B (8.14%), and 1300 nm SLD A+B (8.30%).

In an effort to provide a fully characterized assessment of flow using the different light sources by db-SdOCT methods, flow direction may also be computed by statistical means; inspiration for this was taken from recent work by Wang et al.[61] Autocorrelation methods for quantitative mapping of transverse particle-flow velocity employ the statistical nature of the intensity fluctuation of backscattered light modulated by (stochastically) flowing particles. When a particle traverses a probe beam, relatively strong backscattered light with a pulse width identical to the traverse time, $t_0 = w/v$, results (distinct from the transit time between beams used in cross-correlation computation, t_t — this difference is illustrated in Fig. 4), where w is the transverse size of the probe beam. This results in modulations of the
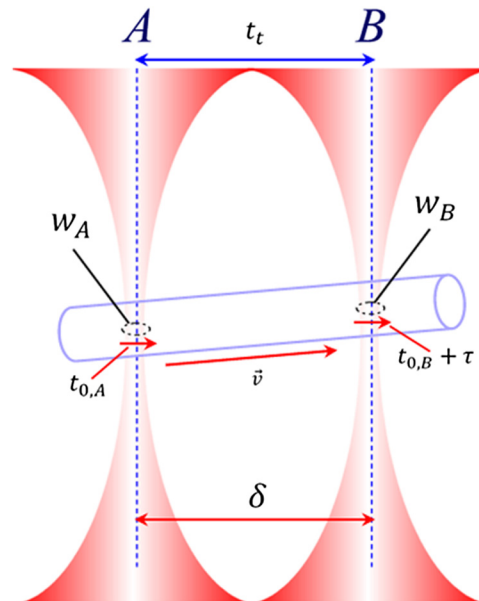

Fig. 4 Illustration of the parameters involved when utilizing autocorrelation analysis for bidirectional studies. A and B refer to each channel of the db-SdOCT system; w denotes the respective beam width; t_0 is the traverse time for each probe beam and t_t is the transit time used in cross-correlation computation (included here for differentiation only, not used in autocorrelation computation); δ is beam separation distance; and $\vec{v}$ indicates velocity direction.

remitted light, which may be approximated as a sequence of rectangle functions.[66] This concept has been used to deduce particle-flow velocity;[67] however, it is unable to discern directional data. As the system described in this work may be likened to a miniature time gate, by utilizing the concepts of autocorrelation and knowing the relative temporal separation (τ) of these beams, it is possible to distinguish which beam the particulate matter under investigation encounters first and thus direction may be discerned; this is outlined in further detail in Ref. 57.

Prior to commencing any experimentation, the initiating channel (i.e., either A or B) is selected (see Fig. 4; in this case, for illustration, A was chosen as the starting channel for acquisition and switching, although in general this is arbitrarily chosen and documented for use in the subsequent analysis).

As autocorrelation computation utilizes the same raw OCT data as for cross-correlation velocity analysis, both algorithms can be implemented simultaneously resulting in only marginal increases in processing time. As with the cross-correlation data, both intensity and phase were tested for their ability to yield directional data. In all autocorrelation computations, the temporal compensation delay factor (β) was incorporated. Directionality studies were also performed on all velocity data, acquisition rates, and capillary sizes. It was found that although all light sources could predict the correct (known *a priori*) directional behavior for phase-based correlation analysis, SLD B performed the best in terms of directional predictions. A sample subset of directionality focal volume experimental values for a 500-μm capillary using all three light sources at OPR33 can be seen in Table 2.

2.3 Light Source Optimization—Discussion

Speckle is the result of the superposition of many random wavelets, whose amplitudes and phases are statistically independent; phases are uniformly distributed over $(-\pi, \pi)$ (only fulfilled if there are sufficient scatterers in the coherence volume) and are perfectly polarized.[68] Speckle properties are affected by sample properties like structure and motion, and by properties of the light source and the sample beam optics. In OCT, the noise aspect of speckle dominates and considerable attention has been paid to methods devoted to speckle reduction. In clinical analyses, OCT speckle can mask diagnostically relevant image features and reduce the accuracy of segmentation algorithms.[69] In industrial metrology, speckle has played an important role in the measurement of surface roughness, strain, and deformation.[70] Generally, however, speckle is treated as an insidious form of noise in OCT and is thus suppressed in most instances. Hence, techniques of suppression/removal of speckle have been reported as hardware and software implementations.[71,72] However, second-order temporal speckle statistics have also been shown to carry information about scatterer motion whose fluctuations have a dependence on the mean velocity;[73] coupled with OCT, this offers the capability of depth-resolved flow profiles with the added benefit of being able to detect motion normal to the OCT axis. However, although Doppler methods can discern directional information, speckle flow measurements cannot.

Different velocity phenomena are present in the above experimental investigations: an increase in cross-correlation velocity value accuracy for increased capillary size, acquisition rate, and certain focal volume considerations. In terms of justifying the trend of increasing accuracy of velocity values gleaned with increasing capillary diameter, this may be understood using the above rationale of speckle OCT. Regions of movement

within a real-time OCT image capture are apparent by the intermittent flickering of the speckle present. As such, in reference to cross-correlation analysis, a sufficient amount of transient speckle OCT data (although this is arbitrary) must be present and detectable within the coherent probe volume (see Fig. 11) of the impinging light beams such that clear computation of like events of high correlation may be realized.

From Fig. 3, it is evident that an increased deviation from theoretically applied flow rates occurs for decreasing capillary size using cross-correlation analysis. Insufficient OCT speckle data within the probing coherent volume at faster velocities makes discernment of instances of high statistical correlation more difficult. However, for the lower values of velocity applied, e.g., 50-μm sizes, such errors are not as prominent and the reduction in sample data from this reduced coherent volume is compensated for by the slower flow rates. Although this may indicate a theoretical upper limit on the assessable velocity range for smaller capillary values, capillaries of this size occurring naturally have much smaller flow rates than those represented by the upper velocity range assessed here. Reported values for red blood corpuscle velocity (RBCv) within capillaries indicate a mean value of 1.85 mm/s (Ref. 4); the experimental flow range was less than and much greater than this value as a test for the capability of the system for biomedical applications in, for example, turbulent conditions for which larger velocity values may be present.

As discussed above, it is evident from the experimental data that there is a fall-off in accuracy for faster flow rates in both the intensity and phase regimes, dependent upon capillary size. Recent imaging applications in wide-field fluorescence and confocal microscopy have increasingly centered on the demanding requirements of recording rapid transient dynamic processes that may be associated with a very small photon signal and that often can only be studied in living cells or tissues. Improvements in camera, laser, and computer hardware have contributed to many breakthrough research accomplishments in a number of fields. As high-performance camera systems employing low-noise cooled CCDs have become more capable of capturing even relatively weak signals at video rates and higher, certain performance factors necessarily take on greater importance. The influence of the acquisition time on the resulting cross-correlation analysis concluded that increasing the line scan rate positively influenced the ability of the cross-correlation algorithm to yield increasingly accurate velocity values. In clinical terms, reducing acquisition times may improve patient throughput, increase camera efficiency, and reduce costs; however, reducing acquisition time also increases image noise,[74] and therefore the ability of the intensity-based methods; thus, the utility of the db-SdOCT method in such instances may prove advantageous.

The detectable velocity dynamic range (VDR) of a phase-resolved DOCT (PrDOCT) system is governed by a detectable Doppler phase shift, a flow angle, and the acquisition interval.

$$\text{VDR} = \frac{\lambda_0}{4T_\eta}\left(\underbrace{\frac{\Delta\phi_{\text{err}}}{\pi}}_{\text{min}} : \underbrace{1}_{\text{max}}\right), \qquad (8)$$

here $\Delta\phi_{\text{err}}$ is the phase error, which can be statistically quantified as the deviation from the mean of the phase difference measured from a stationary sample. Shortening the acquisition duration will increase both the maximum and minimum detectable velocity values; however, this may lead to the invisibility of

Table 2 Experimental values for investigations of flow directionality in a 500-μm *in vitro* sample with 2% intralipid solution for a (a) SLED 1310 nm, (b) 1300 nm SLD A+B, and (c) 1340 nm SLD B light sources at OPR33.

		Autocorrintensity		Autocorrphase		Intensity	Phase
Light sources	Velocity (m/s)	ChA	ChB	ChA	ChB	ChB to ChA flow direction?	ChB to ChA flow direction?
a) SLED	0.0005	0.022563	0.016646	0.021565	0.014086	TRUE	TRUE
	0.001	0.024808	0.016446	0.021585	0.014852	TRUE	TRUE
	0.002	0.0213	0.013837	0.021025	0.013647	TRUE	TRUE
	0.003	0.022554	0.018714	0.023639	0.015145	TRUE	TRUE
	0.004	0.025189	0.040766	0.023881	0.014286	FALSE	TRUE
	0.005	0.024371	0.017537	0.021689	0.013301	TRUE	TRUE
	0.006	0.022116	0.01961	0.025504	0.014776	TRUE	TRUE
	0.007	0.021013	0.02994	0.019352	0.015245	FALSE	TRUE
	0.008	0.024367	0.015409	0.022192	0.015203	TRUE	TRUE
	0.009	0.021173	0.058048	0.021642	0.013602	FALSE	TRUE
	0.01	0.018704	0.015775	0.01922	0.014494	TRUE	TRUE
b) SLD A+B	0.0005	0.022976	0.016561	0.024307	0.012907	TRUE	TRUE
	0.001	0.024864	0.014422	0.021458	0.012825	TRUE	TRUE
	0.002	0.021445	0.019301	0.021506	0.017631	TRUE	TRUE
	0.003	0.021765	0.013831	0.024461	0.017193	TRUE	TRUE
	0.004	0.022398	0.015716	0.021425	0.016979	TRUE	TRUE
	0.005	0.022373	0.016568	0.019994	0.016529	TRUE	TRUE
	0.006	0.022505	0.017289	0.022004	0.014359	TRUE	TRUE
	0.007	0.020723	0.026592	0.021769	0.017164	FALSE	TRUE
	0.008	0.022498	0.016107	0.023111	0.01333	TRUE	TRUE
	0.009	0.023595	0.035832	0.02243	0.015296	FALSE	TRUE
	0.01	0.020302	0.021089	0.019072	0.013432	FALSE	TRUE
c) SLD B	0.0005	0.022845	0.014011	0.021162	0.013939	TRUE	TRUE
	0.001	0.021055	0.01435	0.021413	0.01495	TRUE	TRUE
	0.002	0.022834	0.015811	0.018672	0.014798	TRUE	TRUE
	0.003	0.019563	0.0146	0.019376	0.014049	TRUE	TRUE
	0.004	0.019595	0.015908	0.02363	0.014131	TRUE	TRUE
	0.005	0.022801	0.014017	0.020777	0.014463	TRUE	TRUE
	0.006	0.022688	0.015806	0.021343	0.01468	TRUE	TRUE
	0.007	0.019503	0.013723	0.020171	0.014897	TRUE	TRUE
	0.008	0.019532	0.014678	0.019806	0.014714	TRUE	TRUE
	0.009	0.024065	0.015562	0.022098	0.013804	TRUE	TRUE
	0.01	0.019832	0.014545	0.021309	0.015338	TRUE	TRUE

slow flow. Both the upper and lower limits of the VDR depend on the flow angle when the absolute flow is concerned. In practice, in *in vivo* flow monitoring, the flow orientation may vary from 0 to 90 deg relative to the incident beam, leading to a wide dynamic range of axial flow velocities. Invisibility of slow flow will be more severe when the flow angle approaches 90 deg, which produces extremely slow axial flow. In an effort to surmount the obstacles of VDR using PrDOCT, multiscale measurement protocols have been reported,[75] in which the Doppler phase shifts have been computed along both the fast and slow scanning axes, thus yielding different ranges of detectable flow velocity simultaneously. Methods such as moving scatterer-sensitive SdOCT have reported improved sensitivity over conventional PrDOCT techniques by disregarding the influence of stationary scatterers by subtracting adjacent complex axial scans before calculation of the Doppler frequency shift.[76] However, in terms of db-SdOCT analysis, cross-correlation between two channels (whose data length are N) can provide a maximum time delay of $\pm(N-1)\tau$ and a minimum time delay of $\pm\tau$ ($\pm$ denotes possible opposing directions). As such, the velocity measurement range is

$$\pm\left(\frac{\delta}{(N-1)\tau}\sim\frac{\delta}{\tau}\right),$$

whose parameters could be flexibly set to meet the requirements of a variable velocity measurement range.

The errors associated with the cross-correlation computation of velocity values using (1) SLD A+B and (2) SLD B may be attributable to (1) higher-order dispersion effects and (2) comparatively bad transverse resolution, resulting in an insufficient discernment of speckle data for correlation purposes. Conventional lenses have a focal length that varies with wavelength and thus focus ultra-broadband light to different planes. This variation in focal position for different wavelengths alters the local effective bandwidth and therefore degrades resolution.[74] For specially corrected achromatic optics, different imaging distances introduce a wavelength-independent attenuation of the whole spectrum, thereby maintaining the spectral shape, bandwidth, and, therefore, axial resolution. In an effort to compensate for higher orders of dispersion prominent in the extended SLD A+B source, achromatic lenses were employed in addition to dispersion compensating blocks in the sample and reference(s) arms. However, multiplexed SLD light sources have the disadvantage of having spectrally modulated emission spectra that can produce side lobes in the coherence function, resulting in image artifacts. Therefore, without numerical compensation of such artifacts, ultra-broad bandwidth sources are naturally degraded in terms of resolution. Nevertheless, if such compensation was implemented, the computational requirements for all sources would not be equal and thus could not be compared appropriately for focal volume influence in correlation assessment.

There are several methods by which dispersive effects can be mitigated, e.g., inserting variable-thickness BK7 and fused silica prisms in the reference arm.[77] Second-order or group velocity dispersion can be compensated for by implementing rapid scanning optical delay lines;[78,79] however, higher orders of dispersion are not compensated for. An alternative is dispersion compensation in software by various numerical methods;[80,81] e.g., dispersion can be removed by multiplying the dispersed cross-spectral density function with a phase term $e^{-i\theta(k)}$, which can be derived experimentally.[82] Compensation of higher-order

terms is important only when an ultra-broadband light source is used, which can significantly degrade resolution with increasing bandwidth.

In terms of bidirectionality, it is evident from Table 1 that the resulting transverse resolution of 1340 nm SLD B (theoretically calculated, 34.80 μm) is 2.29 and 3.08% larger than those of the 1310 nm SLED and extended bandwidth SLD A+B, respectively. The increase in the probing coherence volume may be attributed to the improvement seen in the clear distinguishing of direction (see Table 2), considering either intensity- or phase-based correlation analysis as the time taken for flowing media to traverse these probing lengths is justifiably longer both transversely and axially, enabling an increased accuracy regarding the discernment of direction via autocorrelation analysis.

3 *In Vitro* Pulsatile Flow Model Experimental Considerations

Flow is characterized by two dimensionless quantities, the Reynolds number (Re) and the Womersley number (α), defined as

$$\mathrm{Re}=\frac{d\bar{v}\rho}{\vartheta}\quad\text{and}\quad\alpha=d\sqrt{\frac{2\pi f\rho}{\vartheta}}, \qquad (9)$$

where d is the vessel diameter; $\bar{v}$ is the bulk velocity; ρ is the density; ϑ is the dynamic viscosity; and f is the characteristic frequency. Generally, low Reynolds numbers indicate laminar flow rates, whereas for low Womersley values, pulsatile flow is dominated by viscous effects.[83] The nonlinear, transient pulsations in pressure and flow of the cardiovascular flow mechanism results in variations in applied shear stress to vessel walls. Although such flow characteristics may be modeled using Navier–Stokes equations,[84,85] the Womersley number is a convenient dimensionless measure of the pulsatile flow frequency in relation to viscous effects rather than a model of the actual flow. Womersley numbers were calculated using Eq. (9) for 500, 300, 50 μm *in vitro* phantoms, with flowing 2% intralipid solution (see Table 3). In the case of the experimental work outlined here, α values are calculated for the chosen *in vitro* model capillary sizes, see Table 1.

As some typical values for the Womersley number in the cardiovascular system for a canine model ($f = 2$ Hz) are 0.04, 0.035, and 0.005 for arterioles, venules, and capillaries, respectively,[86–88] the calculated experimental values correlate well so as to provide an accurate representation of *in vivo* pulsatile flow. When values for α are small ($\leq$1), this implies that

Table 3 Experimental Womersley numbers, α, using 1060 kg/m³ and 0.006 (Ns/m²) for the density and dynamic viscosity parameters, respectively.

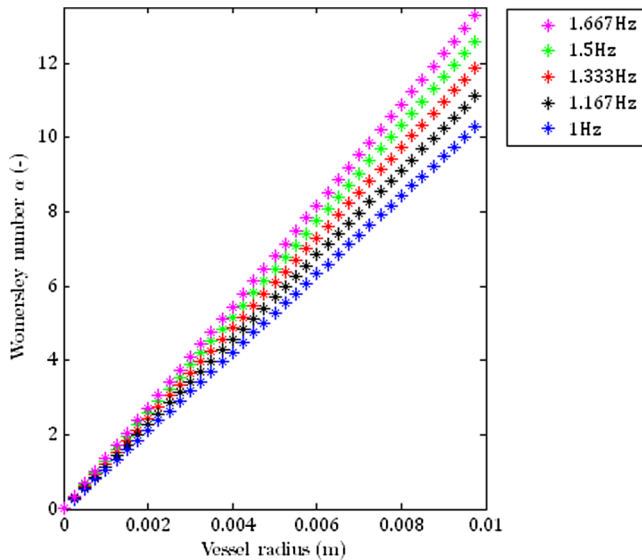| Beats per min	500 μm	300 μm	50 μm
60	0.527	0.316	0.053
70	0.569	0.341	0.057
80	0.608	0.365	0.061
90	0.645	0.387	0.065
100	0.680	0.408	0.068

Fig. 5 Plot of Womersley values (α) versus vessel radius for various values of pulsation frequency. As a heart rate of 60 to 100 beats per minute (bpm) is the criterion for sinus rhythm, such values were investigated in this work.

the frequency of pulsations is sufficiently low that a parabolic (Hagan-Poiseuille flow) velocity profile has time to develop during each cycle; this is illustrated in Fig. 5.

In order to induce pulsations to the applied flow of the *in vitro* model experimental setup, a section was cut in the plastic tubing connecting the syringe pump to the flow phantom, which was placed in the focal plane of the db-SdOCT system. This cut section was replaced with a larger diameter tubing, which had greater malleability (see Fig. 6); this valve regulated and controlled the pulse applied to the phantom and ensured pulse propagation throughout the entire length of the closed system. The pulse was applied using a motive force generator (MFG) (model: mini-shaker 4810; Brüel & Kjær, Denmark), onto which the valve was clamped. A signal generator (Unilab, UK) supplied voltage to the MFG and a square waveform was applied, the frequency of which was monitored with an oscilloscope (model TDS 210; Tektronix, USA). The amplitude of the voltage supplied dictated the extent of the displacement performed by the MFG (maximum displacement, ± 3 mm). It was evident that if the chosen voltage amplitude (peak to peak) was too high, the pressure variations caused by the
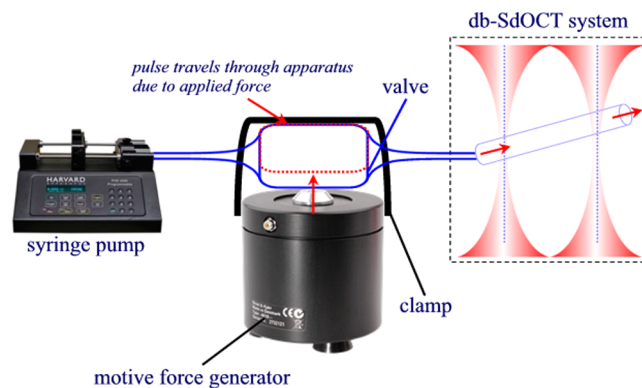
pulse created great turbulence within the phantom. Although intralipid was still flowing under these circumstances, the large amplitude of the pulse voltage impeded the flow, which is not representative of the dynamics present in an *in vivo* biological environment. Consequently, the amplitude was reduced such that the flow was pulsed, but its course was not inhibited by the simulated pulse. Considering the light source optimization investigations as outlined in Sec. 2, the inexpensive SLED 1310-nm light source was used for pulsatility studies.

3.1 *db-SdOCT Algorithm for Extraction of Pulsatile Behavior*

Pulsatile information may be gleaned through either physical measurements or imaging methods. With regard to Doppler-based modalities, a common trend exists in their respective processing of pulsatile information, even though they may be markedly different in the parameters they consider for processing or methods of processing,[89] e.g., phase, variance. Generally, a region may be cropped and transient behavior analyzed by integrating the phase of the demarcated region over time. Power spectral densities may then be obtained by implementing nonparametric methods.[90] Alternately, sequences of flow profiles may be extracted; this serves a dual purpose in that both pulsatility and turbulence may be analyzed if flow profiles depart from the laminar condition (see Fig. 7). However, with regard to the db-SdOCT method, as the method of extracting and analyzing velocity data is dissimilar to the aforementioned methods, an alternative means of extracting pulsatile information is considered.

As described in Sec. 2.1 and in detail elsewhere,[57] velocity values are acquired by cross-correlation computation of intensity and/or phase data using the data obtained by the db-SdOCT system. One method of expanding this algorithm for analysis of pulsatility is to compute the axial velocity profiles for each instant in time and to track the maximum velocity obtained temporally through appropriate fitting. Although possible, this approach would greatly increase the computational expense involved and may be a limiting factor if applied to real-time applications. An alternative approach is to utilize the computed maximal correlation differences in time between channels and to examine this using FFT for any spectral components of interest.

For the pulsatility investigation outlined here, various different flow rates were considered, and five different pulse frequencies were artificially applied to *in vitro* flow phantoms to study whether the pulse affects the db-SdOCT methods' ability to discern velocity data with forced dynamic changes present. In order to increase the resolution of the frequency axis, a larger dataset of A-scans than normal was obtained—this dataset comprised 5000 A-scans with switching time $\tau = 1.59$ ms. To remove artifact ghost lines from each frame, all spectra comprising the image were averaged, generating a single background spectrum. Each individual raw spectrum was divided by this background, removing all fixed pattern noise in the image.[41] OCT and cross-correlation analysis was applied to the data, which corresponded to a total time available for FFT analysis of 3.98 s. The criterion for normal sinus rhythm includes a heart rate range of 60 to 100 beats per minute (bpm) (i.e., a simulated pulse range of 1 to 1.67 Hz). As such, given the total analysis time available, this corresponds to a possibility of detecting between 4 and 6 pulses during any single acquisition.
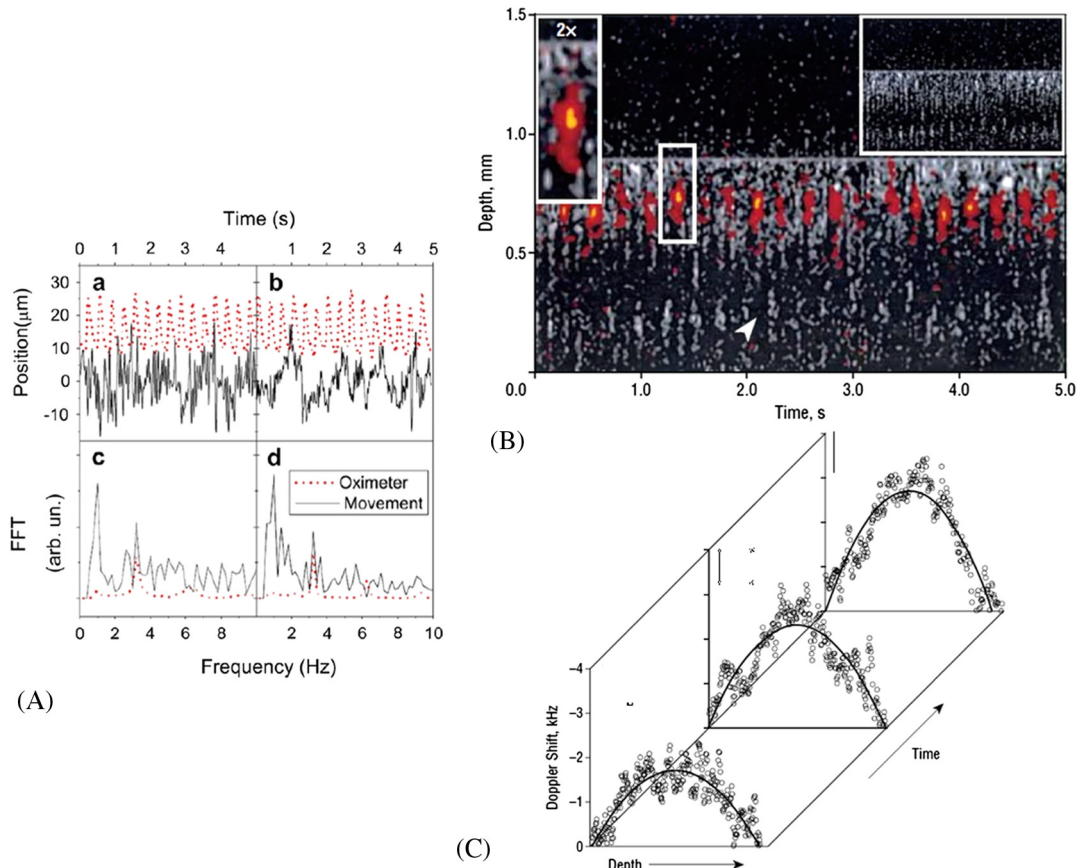

Fig. 6 Illustration of the experimental setup to investigate pulsatile flow phenomena in *in vitro* flow models.

Fig. 7 Example of methods used to yield pulsatile information. (A) Longitudinal retinal (a) and corneal (b) displacements were measured and FFTs were performed on the resulting data [(c) and (d)] revealing the spectral components present.[91,92] and (C) Extraction of retinal flow dynamics by color Doppler OCT: (B) A sequence of two-dimensional images of a selected retinal blood vessel in time. (C) Extracted axial flow profiles revealing the maximal Doppler shift changes with time.[47]

3.2 Pulsatile Analysis Results—Discussion

Experimental investigations involved *in vitro* capillary models of sizes 500, 300, and 50 µm with flow rates of the range 1 to 11 mm/s (in increments of 2 mm/s), performing both cross-correlation analysis (for velocity quantification) and FFT computation (for spectral analysis) using both intensity and phase data (see Fig. 9). With regard to the cross-correlation velocity data for all capillary sizes, deviation from the theoretical velocity values supplied by the syringe pump were 3.57 and 3.18% for intensity- and phase-based analysis, respectively, indicating (1) the application of the simulated pulse did not impede the ability of the system or its associated algorithms to yield velocity values representative of the applied flow rates and (b) the advantageous use of the phase as the cross-correlation metric in dynamic assessment (see Fig. 10).

Insufficient OCT speckle data within the probing coherent volume at faster velocities makes discernment of instances of high statistical correlation more difficult. As such, an increased deviation from theoretically applied flow rates occurs for decreasing capillary size using cross-correlation analysis.[57] In terms of justifying the trend of increasing accuracy of velocity values gleaned with increasing capillary diameter, this may be understood using the rationale of speckle OCT. Regions of movement within a real-time OCT image capture are apparent by the intermittent flickering of the speckle present. Resultantly, in reference to db-SdOCT cross-correlation analysis, a sufficient amount of transient speckle OCT data (although this is arbitrary)

must be present and detectable within the coherent probe volume (see Fig. 11) of the impinging light beams, such that clear computation of like events (i.e., instances of high correlation) may be realized.

However, for lower values of velocity, e.g., 50-µm sizes, the reduction in speckle data available from the resultant reduced coherent volume is compensated for by the slower applied flow rates (i.e., flow rates in 50-µm-diameter capillaries are 10^2 smaller than in 500-µm sizes). Reported values for RBCv within capillaries indicate a mean value of 1.85 mm/s (Ref. 4); the experimental flow range demonstrated in this work was less than and much greater than this value as a test for the capability of the system for biomedical applications in, for example, turbulent conditions for which larger velocity values may be present.

In reference to FFT analysis of the simulated *in vitro* pulses, smaller capillary diameter sizes result in better discernment and consistency of the pulsatile values computed (see Fig. 12). This stems from the fact that although slower flow rates are applied, any temporal change in the volume of flowing media in such smaller capillary sizes is more appreciable, thereby enabling pulsatile detection with greater efficacy. In general, however, it was clear from the resulting analysis that the errors relating to the values of the FFT maximum frequency obtained increased as the applied velocity values decreased. The mean error of the detected simulated pulsations for the three quoted capillary sizes over the velocity range of 1 to 11 mm/s (in increments of
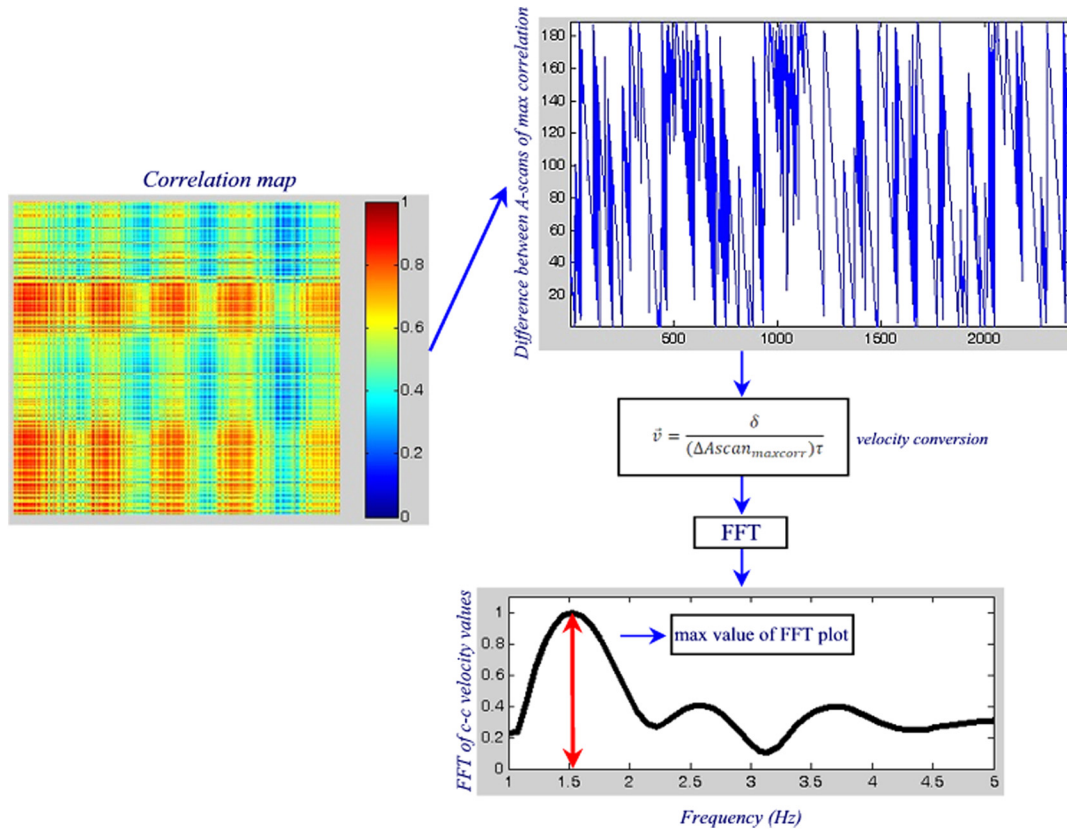
Fig. 8 Illustration of the processing procedure used to extract pulsatile flow information from an *in vitro* flow model with simulated pulsations applied. Velocity data are computed from cross-correlation temporal map values (an in-depth description of this procedure is outlined elsewhere[57]) and an FFT is performed. Harmonics are also evident in the resulting data.
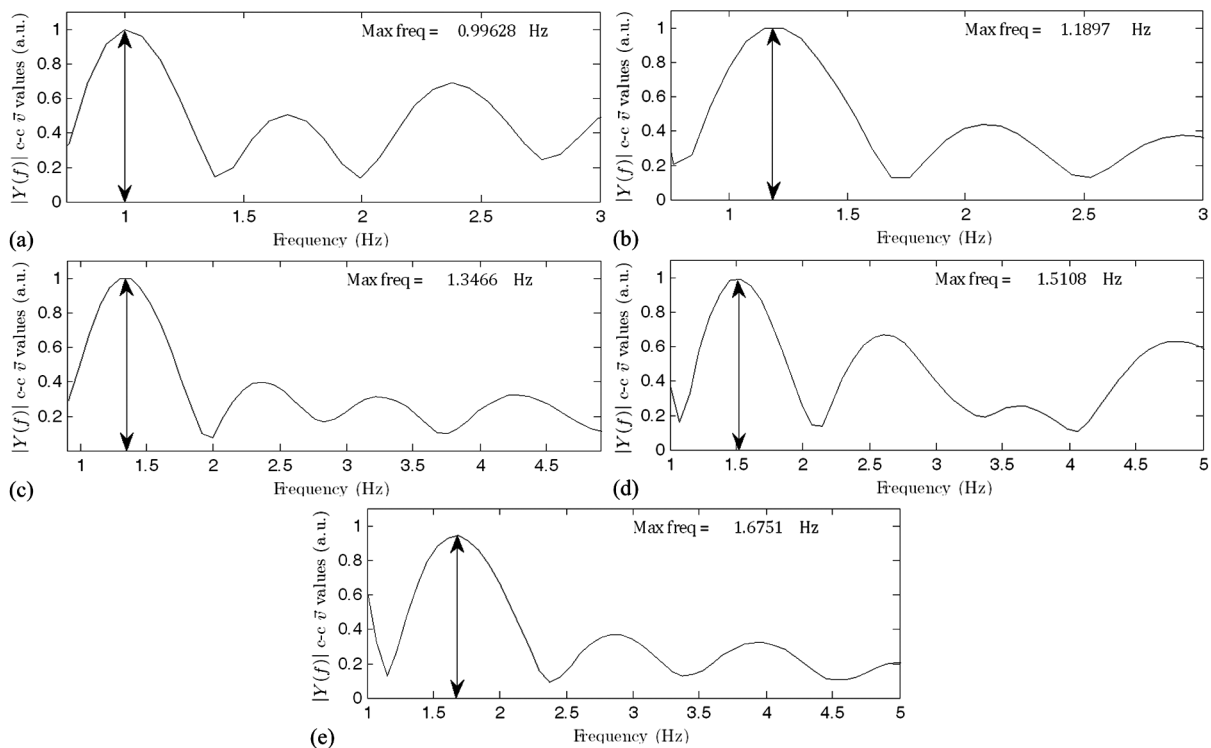

Fig. 9 FFT analysis of intensity-based cross-correlation velocity data for simulated *in vitro* pulses in a 300-μm capillary with flowing 2% intralipid solution at 11 mm/s. The pulse values ranged from 60 to 100 bpm in increments of 10 bpm, i.e., (a) to (e) respectively, corresponding to the frequency range present in cardiac sinus rhythm. The pulse frequency values detected correspond to <0.8% deviation from the simulated pulse frequencies applied.
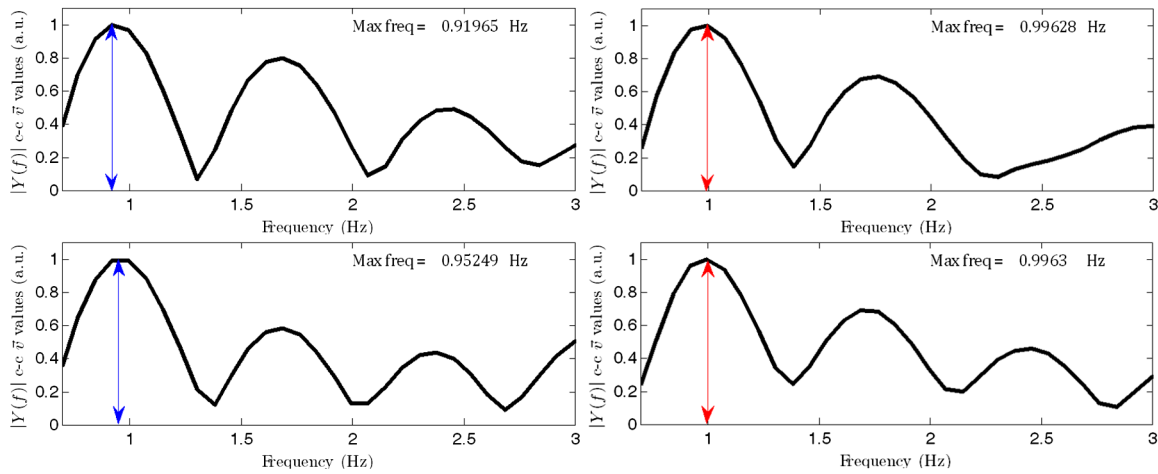
Fig. 10 FFT analysis of (top) 500 μm and (bottom) 50 μm capillary with flowing 2% intralipid solution at 7 mm/s with a simulated pulse of 60 bpm. Both (left) intensity and (right) phase-based cross-correlation velocity values were used. Phase-based analysis demonstrated decreased error in its replication of simulated pulse values. In the above examples, the relative errors were (intensity, left) 500 μm = 8.40%, 50 μm = 5.13%; and (phase, right) 500 μm = 0.8%, 50 μm = 0.77%.
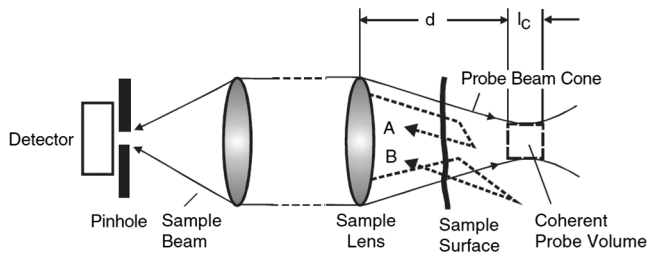

Fig. 11 Geometry of a single sample beam illustrating the coherent probe volume.[4]

2 mm/s) is 9.43% [Fig. 12(a)] and 6.52% [Fig. 12(b)] based on FFT analysis resulting from, respectively, intensity- and phase-based cross-correlation velocity data. This point is also highlighted in Fig. 13, in which for the same applied flow rate, the errors relating to the position of the resulting maximal frequency obtained increased with decreased simulated applied pulse.

As velocities decrease, the time to travel between ChA and ChB of the db-SdOCT system increases with decreasing velocity, and this is reflected in the cross-correlation analysis, requiring more data for computation of velocity values. This reduction in flow velocity speed may also impede the ability to discern pulses, resulting in inevitable errors in the FFT analysis. This perhaps indicates a limitation involved with applying FFT to cross-correlation yielded velocity data, but this may also be attributed to the unrealistic inelastic expansion of the *in vitro*
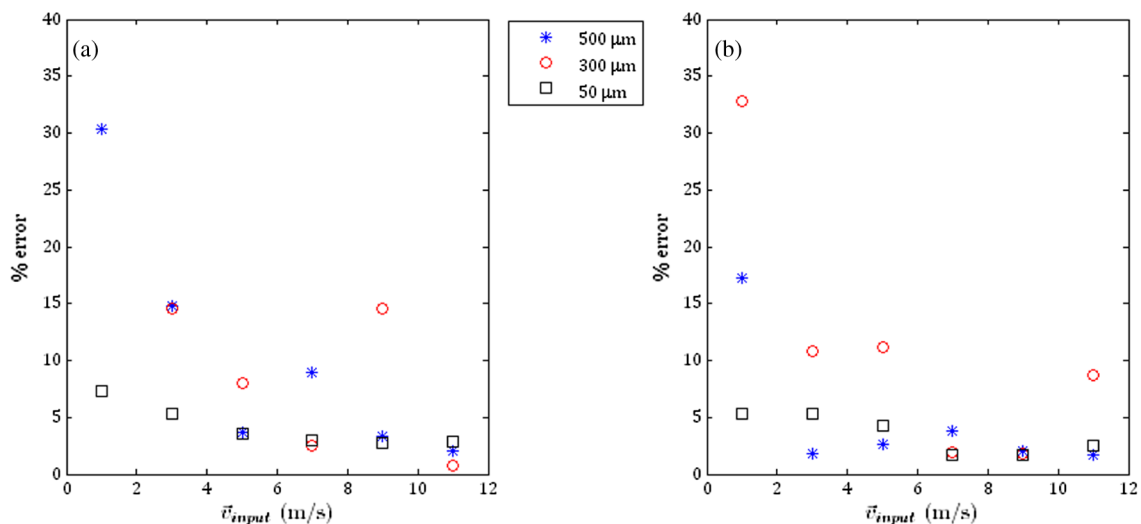

Fig. 12 In pulsatile FFT analysis, an evident error increase in the location of the FFT maximum occurred with decreasing velocity values. The above plots reveal the % error obtained for the maximal correlation frequency and the simulated applied pulse for (a) intensity and (b) phase-based correlation analysis. The errors obtained were more prominent for larger capillary sizes at lower flow rates. (A second-order polynomial fit is shown for trend clarity.)
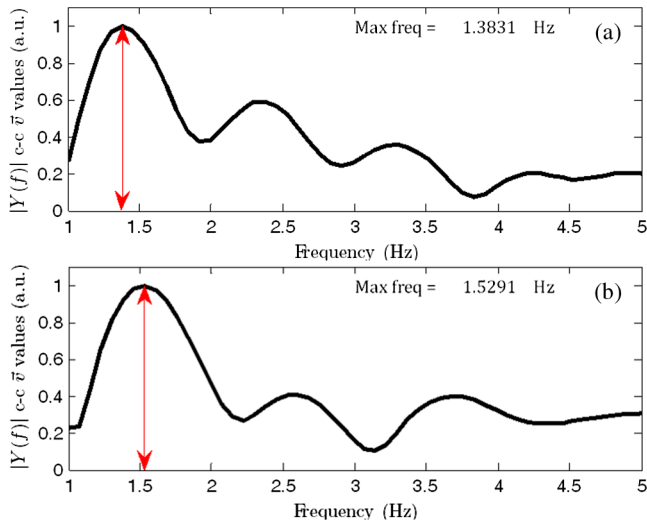
Fig. 13 An increased error in the location of the FFT maximum occurred with decreasing pulse frequencies. The data show a 500-μm capillary with flowing 2% intralipid solution at 9 mm/s at (a) 80 bpm and (b) 90 bpm, representing a respective deviation of 4.31 and 2.14% from the simulated pulse frequency applied. (Intensity-based cross-correlation velocity data are used in FFT computation.)

flow model implemented. Regular expansion of biological vessels assists in the regulation of pulsatile flow patterns; the rigidity of the silica capillaries, therefore, may not be a realistic analogue. Thus, although this is a possible limiting aspect to the db-SdOCT method and algorithm for *in vitro* investigations, the naturally occurring elasticity of the *in vivo* biological environment lends credibility to its use.

Higher harmonics are evident in the resulting FFT plots, which is unsurprising as the cross-correlation-derived velocity values exhibit sharp corners and steep slopes in the time domain (see Fig. 8). Although the resulting maximal pulsations rise well above the noise floor, this may prove problematic in distinguishing the maximum dynamic frequency present with decreasing velocity values. A smoothing filter prior to FFT processing performed on the resulting correlation data could mitigate these effects; however, the influence of the use of such filtering on correlation data would require further investigation.

The computed temporal maps of the cross-correlation velocity data revealed some turbulent changes to the flow investigated if increased pulse frequencies were applied. Figure 14 demonstrates the increased turbulent behavior present due to higher pulse frequencies at the same applied flow rate in the resulting temporal cross-correlation maps.
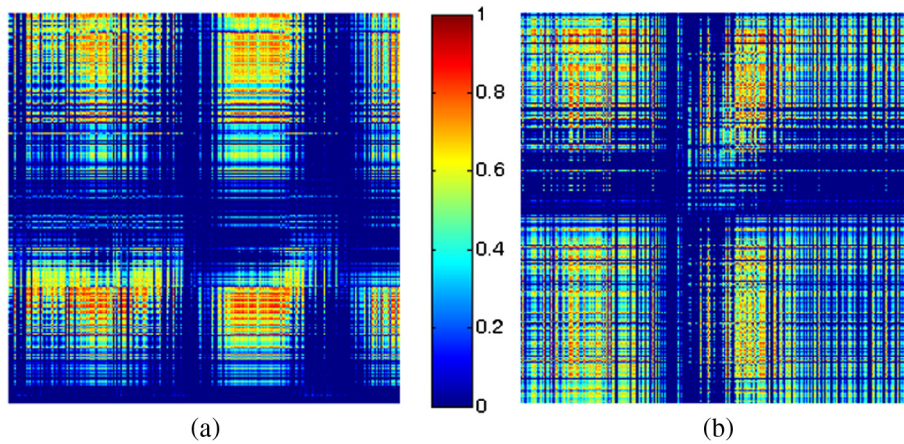

Fig. 14 Temporal cross-correlation maps resulting from analysis of a 50-μm capillary with flowing 2% intralipid at 5 mm/s with simulated pulse at (a) 60 bpm and (b) 100 bpm. The increased pulse frequency resulted in a more turbulent correlation map.
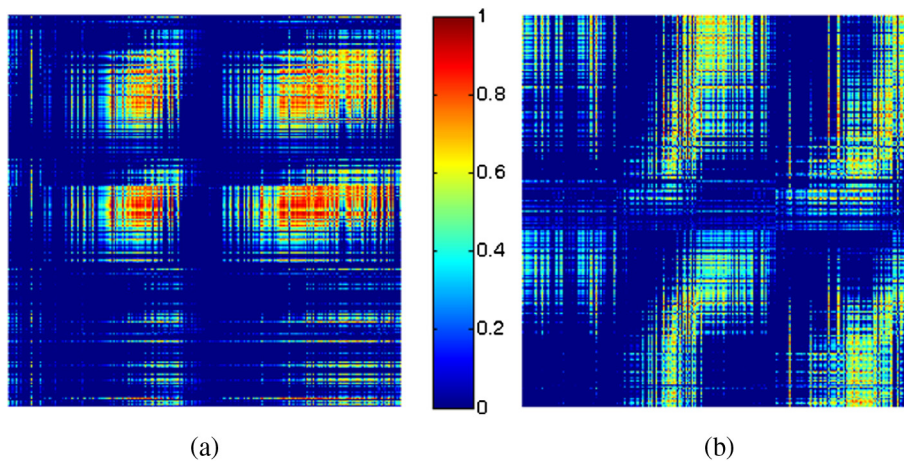

Fig. 15 50-μm capillary with a simulated pulse at 60 bpm with flowing 2% intralipid solution at (a) 9 mm/s and (b) 11 mm/s. Although both images reveal temporally segmented regions of high correlation, this illustrates the effect of increasing velocity on correlation plots. The slow flow rates applied to the 50-μm capillary enable the capture of this phenomena in comparison to 500-μm capillaries in which establishment of 9 or 11 mm/s requires flow rates 10^2 larger.

However, this disturbance had only a minor effect on the ability of the db-SdOCT algorithm at discerning velocity data, with an overall difference between an applied pulse of 60 and 100 bpm for all velocity values (and considering all capillary sizes) of 0.19%. This may be juxtaposed to the previously described analysis of Fig. 12, in which the applied flow rates impacted on the discernment of applied pulse values. This reveals that the converse is untrue. Similar effects in the rendered temporal correlation maps result if increasing velocities are considered at a set simulated pulse rate (see Fig. 15).

4 Conclusion

Presented here is a detailed outline of the construction, application, and optimization of the associated processing procedures of the db-SdOCT methodology for the functional assessment of *in vitro* flow of simulated sinus rhythm. By monitoring intensity fluctuations, it is possible to derive information about the motion of scattering particles present. This method utilizes the statistical aspects of OCT data to yield velocity values and its stochastic nature to discern direction. This reveals the db-SdOCT method to be a multifaceted modality capable of discerning and quantifying a variety of functional aspects evident in *in vivo* environments.

In highly scattering turbid media, spectral broadening may induce errors in the calibrated values for the beam size and ergo relative sample beam separation values, especially if the specimen is not placed approximately within the focal plane. In addition, the initial choice of focal volume size (i.e., $l_C \times \Delta x$) may also play a part in the introduction of unnecessary errors to the cross-correlation computation. Considering the higher-order dispersive effects evident in ultra-broad bandwidth sources, the variation in longitudinal and transverse resolution values, and the penetrative depth of field differences, the effects of such spectral characteristics are assessed individually using the db-SdOCT system and subsequent cross-correlation processing for velocity quantification and discernment of directionality. Practical implementation of cross-correlation analysis to yield velocity data was best achieved by using an inexpensive light source and does not require additional hardware amendments or computational compensation to mitigate for dispersion effects. As such, adaptation of this method into existing OCT setups is relatively straightforward and a cost-effective means of dynamic assessment free from angularly induced artifacts.

Regions of movement within a real-time OCT image capture are apparent by the intermittent flickering of the speckle present. With regard to db-SdOCT cross-correlation optimization analysis and pulsatility investigations, a sufficient amount of transient speckle OCT data must be present and detectable within the coherent probe volume of the impinging light beams, such that clear computation of instances of high correlation may be realized. Therefore, in general, an increase in the accuracy of velocity values gleaned with increasing capillary diameter occurs. However, in terms of extracting pulsatility information, smaller capillary diameter sizes result in better discernment of the pulsatile behavior present; this stems from the fact that although slower flow rates are applied (and are more prone to error in correlation velocity analysis), any temporal change in the volume of flowing media in such comparatively smaller capillary sizes is more appreciable, enabling pulsatile detection with greater efficacy. Although errors relating to the detected maximal pulse frequency increased for slower flow rates, this may be attributed to the *in vitro* flow models implemented.

Slower rates may not transmit the pulsatility information as efficiently for optical acquisition and detection as faster rates would. In addition, the elastic nature of *in vivo* vessels implies that the presence of pulsatile behavior would induce changes in shear stress applied to vessel walls and thus serve to propagate pulsatile phenomena with greater effectiveness. The computed temporal maps of the cross-correlation velocity data revealed some turbulent changes to the flow investigated if increased pulse frequencies were applied. However, these disturbances had only a minor effect on the ability of the db-SdOCT algorithm at discerning velocity data.

The presence of higher harmonics in the resulting FFT analysis may cause issues in the differentiation of the maximum dynamic frequency present, particularly with decreasing velocity values. As such, the application of a smoothing filter prior to FFT processing performed on the resulting correlation data could mitigate these effects; however, the influence of the use of such filtering requires further investigation.

As the experimentation performed in this work concentrated on the intraluminal data within the capillary, demarcation of the capillary from its surrounding turbid medium was required. Although this is straightforward *in vitro*, *in vivo* analysis may pose greater challenges. In terms of quantifying flow *in vitro*, the phase data outperformed the intensity most likely attributed to the inherent stability associated with SdOCT systems. Despite the challenge of achieving high phase stability, swept-source OCT (SsOCT) systems exhibit less fringe wash-out and faster imaging speeds compared to SdOCT detection. Recently, the application of vertical cavity surface-emitting laser light sources to SsOCT operation has been reported,[93] enabling the measurement of pulsatile total retinal blood flow with high sensitivity and phase stability. However, despite this, the intensity information is also of interest as it can be applied to, e.g., cellular systems, which can take advantage of the fact that it is sensitive to the aggregation of biomolecules.[94]

The study of the mutual effect and interactions of the blood flow with the surrounding vessel geometry is of great interest in biorheology and cardiology. The present study demonstrates the potential of discerning pulsatile flow behaviors using an in-house Sd-OCT system with dual-beam configuration for velocity estimation by quasi-simultaneously measuring two planes of illumination, thus obviating the requirement of *a priori* angular knowledge. A succinct outline of the instrumentation and an in-depth description of the related algorithms of the db-SdOCT method and its optimization are provided. The adoption of this methodology into the clinic could become a valid support for intravital exploratory procedures and in general routine assessment, in harmony with its noninvasive premise.

References

1. J. F. Arevalo, C. F. Fernandez, and R. A. Garcia, "Optical coherence tomography characteristics of choroidal metastasis," *Ophthalmology* 112(9), 1612–1619 (2005).

2. I. Svorenova, P. Strmen, and Z. Olah, "Optical coherence tomography—a new imaging method in ophthalmology," *Bratisl. Lek. Listy* **111**(5), 306–307 (2010).

3. G. Guagliumi et al., "Optical coherence tomography assessment of in vivo vascular response after implantation of overlapping bare-metal and drug-eluting stents," *JACC Cardiovasc. Interv.* **3**(5), 531–539 (2010).

4. A. F. Fercher et al., "Optical coherence tomography—principles and applications," *Rep. Prog. Phys.* **66**(2), 239–303 (2003).

5. L. P. Hariri et al., "Laparoscopic optical coherence tomography imaging of human ovarian cancer," *Gynecol. Oncol.* **114**(2), 188–194 (2009).

6. H. J. Boehringer et al., "Imaging of human brain tumor tissue by near-infrared laser coherence tomography," *Acta Neurochir.* **151**(5), 507–517 (2009).

7. E. V. Zagaynova et al., "In vivo optical coherence tomography feasibility for bladder disease," *J. Urol.* **167**(3), 1492–1496 (2002).

8. S. A. Boppart, "Optical coherence tomography—principles, applications and advances," *Minerva Biotecnol.* **16**(4), 211–237 (2004).

9. S. Mordon et al., "Optical coherence computed tomography in gastroenterology," *Gastroenterol. Clin. Biol.* **29**(5), 618–620 (2005).

10. T. Gambichler, V. Jaedicke, and S. Terras, "Optical coherence tomography in dermatology: technical and clinical aspects," *Arch. Dermatol. Res.* **303**(7), 457–473 (2011).

11. J. Welzel, "Optical coherence tomography in dermatology: a review," *Skin Res. Technol.* **7**(1), 1–9 (2001).

12. C. Gimbel, "Optical coherence tomography diagnostic imaging," *Gen. Dent.* **56**(7), 750–757 (2008).

13. L. L. Otis et al., "Optical coherence tomography: a new imaging technology for dentistry," *J. Am. Dent. Assoc.* **131**(4), 511–514 (2000).

14. C. Pitris et al., "High-resolution imaging of gynecologic neoplasms using optical coherence tomography," *Obst. Gynecol.* **93**(1), 135–139 (1999).

15. M. Ascencio et al., "The role and value of optical coherence tomography in gynecology," *J. Gynecol. Obstet. Biol. Reprod.* **36**(8), 749–755 (2007).

16. B. Dunmire et al., "Cross-beam vector Doppler ultrasound for angle-independent velocity measurements," *Ultrasound Med. Biol.* **26**(8), 1213–1235 (2000).

17. M. Rossow, W. W. Mantulin, and E. Gratton, "Spatiotemporal image correlation spectroscopy measurements of flow demonstrated in microfluidic channels," *J. Biomed. Opt.* **14**(2), 024014 (2009).

18. L. V. Wang and H.-I. Wu, *Biomedical Optics: Principles and Imaging*, Wiley, Hoboken, NJ (2007).

19. R. K. Wang et al., "Three dimensional optical angiography," *Opt. Express* **15**(7), 4083–4097 (2007).

20. R. K. Wang and L. An, "Doppler optical micro-angiography for volumetric imaging of vascular perfusion in vivo," *Opt. Express* **17**(11), 8926–8940 (2009).

21. A. Needles et al., "Interframe clutter filtering for high frequency flow imaging," *Ultrasound Med. Biol.* **33**(4), 591–600 (2007).

22. X. Liu et al., "Spectroscopic-speckle variance OCT for microvasculature detection and analysis," *Biomed. Opt. Express* **2**(11), 2995–3009 (2011).

23. A. Mariampillai et al., "Speckle variance detection of microvasculature using swept-source optical coherence tomography," *Opt. Lett.* **33**(13), 1530–1532 (2008).

24. N. Sudheendran et al., "Speckle variance OCT imaging of the vasculature in live mammalian embryos," *Laser Phys. Lett.* **8**(3), 247–252 (2011).

25. J. Fingler et al., "Mobility and transverse flow visualization using phase variance contrast with spectral domain optical coherence tomography," *Opt. Express* **15**(20), 12636–12653 (2007).

26. K. K. C. Lee et al., "Real-time speckle variance swept-source optical coherence tomography using a graphics processing unit," *Biomed. Opt. Express* **3**(7), 1557–1564 (2012).

27. N. A. Fomin, *Speckle Photography for Fluid Mechanics Measurements*, Springer, Berlin, Heidelberg (1998).

28. J. W. Goodman, *Speckle Phenomena in Optics: Theory and Applications*, Roberts & Co., Berlin (2006).

29. M. J. Leahy et al., "Biophotonic methods in microcirculation imaging," *Med. Laser Appl.* **22**(2), 105–126 (2007).

30. K. R. Forrester et al., "Comparison of laser speckle and laser Doppler perfusion imaging: measurement in human skin and rabbit articular tissue," *Med. Biol. Eng. Comput.* **40**(6), 687–697 (2002).

31. K. R. Forrester et al., "Endoscopic laser imaging of tissue perfusion: new instrumentation and technique," *Lasers Surg. Med.* **33**(3), 151–157 (2003).

32. C. J. Stewart et al., "Kinetics of blood flow during healing of excisional full-thickness skin wounds in pigs as monitored by laser speckle perfusion imaging," *Skin Res. Technol.* **12**(4), 247–253 (2006).

33. P. Zakharov et al., "Quantitative modeling of laser speckle imaging," *Opt. Lett.* **31**(23), 3465–3467 (2006).

34. D. L. Kolin and P. W. Wiseman, "Advances in image correlation spectroscopy: measuring number densities, aggregation states, and dynamics of fluorescently labeled macromolecules in cells," *Cell Biochem. Biophys.* **49**(3), 141–164 (2007).

35. Y. Wang and R. K. Wang, "Measurement of particle concentration in flow by statistical analyses of optical coherence tomography signals," *Opt. Lett.* **36**(11), 2143–2145 (2011).

36. S. M. Daly and M. J. Leahy, "'Go with the flow': a review of methods and advancements in blood flow imaging," *J. Biophoton.* **6**(3), 217–255 (2012).

37. K. Bizheva et al., "Imaging ex vivo healthy and pathological human brain tissue with ultra-high-resolution optical coherence tomography," *J. Biomed. Opt.* **10**(1), 011006 (2005).

38. V. X. D. Yang and I. A. Vitkin, *Handbook of Optical Coherence Tomography in Cardiology*, Taylor and Francis Medical, Oxford, UK (2006).

39. R. Iezzi et al., "Proximal aneurysmal neck: dynamic ECG-gated CT angiography-conformational pulsatile changes with possible consequences for endograft aizing," *Radiology* **260**(2), 591–598 (2011).

40. D. D. Duncan et al., "Absolute blood velocity measured with a modified fundus camera," *J. Biomed. Opt.* **15**(5), 056014 (2010).

41. S. Yazdanfar, A. M. Rollins, and J. A. Izatt, "In vivo imaging of human retinal flow dynamics by color Doppler optical coherence tomography," *Arch. Ophthalmol.* **121**(2), 235–239 (2003).

42. A. Shiote, "Effect of deep hypothermia under total spinal anesthesia on blood flow distribution of cardiac output in dogs," *Okayama Igakkai Zasshi* **104**(1–2), 151–164 (1992).

43. E. Ghersin et al., "Pseudoaneurysm of the mitral-aortic intervalvular fibrosa following aortic valve replacement—diagnosis and dynamic evaluation with multidetector CT and transesophageal echocardiography," *Interact. Cardiovasc. Thorac. Surg.* **4**(6), 502–504 (2005).

44. B. R. White et al., "In vivo dynamic human retinal blood flow imaging using ultra-high-speed spectral domain optical Doppler tomography," *Opt. Express* **11**(25), 3490–3497 (2003).

45. A. Aydin et al., "Evaluating pulsatile ocular blood flow analysis in normal and treated glaucomatous eyes," *Am. J. Ophthalmol.* **136**(3), 448–453 (2003).

46. L. Schmetterer and G. Garhofer, "How can blood flow be measured?," *Surv. Ophthalmol.* **52**(2), S134–S138 (2007).

47. K. Singh et al., "Development of a novel instrument to measure the pulsatile movement of ocular tissues," *Exp. Eye Res.* **91**(1), 63–68 (2010).

48. K. Singh et al., "Measurement of ocular fundus pulsation in healthy subjects using a novel Fourier-domain optical coherence tomography," *Invest. Ophthalmol. Vis. Sci.* **52**(12), 8927–8932 (2011).

49. V. X. D. Yang et al., "High speed, wide velocity dynamic range Doppler optical coherence tomography (Part I): System design, signal processing, and performance," *Opt. Express* **11**(7), 794–809 (2003).

50. L. An et al., "High-resolution 1050 nm spectral domain retinal optical coherence tomography at 120 kHz A-scan rate with 6.1 mm imaging depth," *Biomed. Opt. Express* **4**(2), 245–259 (2013).

51. B. H. Park et al., "Real-time fiber-based multi-functional spectral-domain optical coherence tomography at 1.3 mu m," *Opt. Express* **13**(11), 3931–3944 (2005).

52. M. W. Jenkins et al., "Measuring hemodynamics in the developing heart tube with four-dimensional gated Doppler optical coherence tomography," *J. Biomed. Opt.* **15**(6), 066022 (2010).

53. W. Choi et al., "Measurement of pulsatile total blood flow in the human and rat retina with ultrahigh speed spectral/Fourier domain OCT," *Biomed. Opt. Express* **3**(5), 1047–1061 (2012).

54. I. Grulkowski et al., "Retinal, anterior segment and full eye imaging using ultrahigh speed swept source OCT with vertical-cavity surface emitting lasers," *Biomed. Opt. Express* **3**(11), 2733–2751 (2012).

55. W. Drexler, "Ultrahigh-resolution optical coherence tomography," *J. Biomed. Opt.* **9**(1), 47–74 (2004).

56. W. Drexler and J. G. Fujimoto, "State-of-the-art retinal optical coherence tomography," *Prog. Retin. Eye Res.* **27**(1), 45–88 (2008).
57. S. M. Daly, C. Silien, and M. J. Leahy, "Feasibility of capillary velocity assessment by statistical means using dual-beam spectral-domain optical coherence tomography: a preliminary study," *J. Biophoton.* **6**(9), 718–732 (2013).
58. P. M. T. Broersen, *Automatic Autocorrelation and Spectral Analysis*, Springer-Verlag, London (2006).
59. K. Wang and Z. Ding, "Spectral calibration in spectral domain optical coherence tomography," *Chin. Opt. Lett.* **6**(12), 902–904 (2008).
60. S. Reith et al., "Relationship between optical coherence tomography derived intraluminal and intramural criteria and haemodynamic relevance as determined by fractional flow reserve in intermediate coronary stenoses of patients with type 2 diabetes," *Heart* **99**(10), 700–707 (2013).
61. J. A. Izatt et al., "In vivo bidirectional color Doppler flow imaging of picoliter blood volumes using optical coherence tomograhy," *Opt. Lett.* **22**(18), 1439–1441 (1997).
62. J. M. Schmitt, "Optical coherence tomography (OCT): a review," *IEEE J. Sel. Topics Quantum Electron.* **5**(4), 1205–1215 (1999).
63. A. F. Fercher, K. Mengedoht, and W. Werner, "Eye-length measurement by interferometry with partially coherent-light," *Opt. Lett.* **13**(3), 186–188 (1988).
64. J. P. Marfice and O. R. Baiocchi, "Dispersion approximation using higher-order Taylor-series terms," *Appl. Opt.* **26**(19), 4043–4045 (1987).
65. C. K. Hitzenberger et al., "Dispersion effects in partial coherence interferometry: implications for intraocular ranging," *J. Biomed. Opt.* **4**(1), 144–151 (1999).
66. Y. Wang and R. K. Wang, "Autocorrelation optical coherence tomography for mapping transverse particle-flow velocity," *Opt. Lett.* **35**(21), 3538–3540 (2010).
67. H. Asai, "Proposal of a simple method of fluorescence correlation spectroscopy for measuring the direction and magnitude of a flow of fluorophores," *Japn. J. Appl. Phys.* **19**(11), 2279–2282 (1980).
68. P. M. T. Broersen, "Historical misconceptions in autocorrelation estimation," *IEEE Trans. Instrum. Meas.* **56**(4), 1189–1197 (2007).
69. W. Drexler and J. G. Fujimoto, *Optical Coherence Tomography: Technology and Applications*, Springer-Verlag, Heidelberg, Berlin (2008).
70. M. Mogensen et al., "Improved quality of optical coherence tomography imaging of basal cell carcinomas using speckle reduction," *Exp. Dermatol.* **19**(8), E293–E295 (2010).
71. R. Jones and C. Wykes, *Holographic and Speckle Interferometry*, Cambridge University Press, Cambridge (1983).
72. A. Hojjatoleslami and M. R. N. Avanaki, "OCT skin image enhancement through attenuation compensation," *Appl. Opt.* **51**(21), 4927–4935 (2012).
73. M. Bashkansky and J. Reintjes, "Statistics and reduction of speckle in optical coherence tomography," *Opt. Lett.* **25**(8), 545–547 (2000).
74. J. H. Jeong et al., "Measurement of RBC deformation and velocity in capillaries in vivo," *Microvasc. Res.* **71**(3), 212–217 (2006).
75. P. Meemon and J. P. Rolland, "Swept-source based, single-shot, multi-detectable velocity range Doppler optical coherence tomography," *Biomed. Opt. Express* **1**(3), 955–966 (2010).
76. H. W. Ren et al., "Real-time in vivo blood-flow imaging by moving scatterer-sensitive spectral-domain optical Doppler tomography," *Opt. Lett.* **31**(7), 927–929 (2006).
77. P. Puvanathasan et al., "High-speed, high-resolution Fourier-domain optical coherence tomography system for retinal imaging in the 1060 nm wavelength region," *Opt. Lett.* **33**(21), 2479–2481 (2008).
78. G. J. Tearney, B. E. Bouma, and J. G. Fujimoto, "High-speed phase- and group-delay scanning with a grating-based phase control delay line," *Opt. Lett.* **22**(23), 1811–1813 (1997).
79. M. T. Tsai et al., "Dispersion compensation in optical coherence tomography with a prism in a rapid-scanning optical delay line," *Opt. Quantum Electron.* **37**(13–15), 1199–1212 (2005).
80. J. Li et al., "Performance and scalability of Fourier domain optical coherence tomography acceleration using graphics processing units," *Appl. Opt.* **50**(13), 1832–1838 (2011).
81. C. W. Lu et al., "Resolution improvement in optical coherence tomography with segmented spectrum management," *Opt. Quantum Electron.* **37**(13–15), 1165–1173 (2005).
82. B. Cense et al., "Ultrahigh-resolution high-speed retinal imaging using spectral-domain optical coherence tomography," *Opt. Express* **12**(11), 2435–2447 (2004).
83. P. Vennemann, R. Lindken, and J. Westerweel, "In vivo whole-field blood velocity measurement techniques," *Exp. Fluids* **42**(4), 495–511 (2007).
84. W. W. Jeong and K. Rhee, "Effects of surface geometry and non-Newtonian viscosity on the flow field in arterial stenoses," *J. Mech. Sci. Technol.* **23**(9), 2424–2433 (2009).
85. J. S. Stroud, S. A. Berger, and D. Saloner, "Influence of stenosis morphology on flow through severely stenotic vessels: implications for plaque rupture," *J. Biomech.* **33**(4), 443–455 (2000).
86. L. Formaggia et al., "On the coupling of 3D and 1D Navier-Stokes equations for flow problems in compliant vessels," *Comput. Methods Appl. Mech. Eng.* **191**(6–7), 561–582 (2001).
87. A. Quarteroni, L. Formaggia, and N. Ayache, "Mathematical modelling and numerical simulation of the cardiovascular system," in *Handbook of Numerical Analysis*, N. Ayache, Ed., pp. 1–127, Elsevier, Frankfurt (2004).
88. K. Perktold and D. Hilbert, "Numerical simulation of pulsatile flow in a carotid bifurcation model," *J. Biomed. Eng.* **8**(3), 193–199 (1986).
89. Y. C. Fung, *Biomechanics—Motion, Flow, Stress and Growth*, Springer-Verlag, New York (1990).
90. E. D. Ubeyli and I. Guler, "Spectral analysis of internal carotid arterial Doppler signals using FFT, AR, MA, and ARMA methods," *Comput. Biol. Med.* **34**(4), 293–306 (2004).
91. P. D. Welch, "Use of fast Fourier transform for estimation of power spectra—a method based on time averaging over short modified periodograms," *IEEE Trans. Audio Electroacoust.* **15**(2), 70–73 (1967).
92. T. P. Bronez, "On the performance advantage of multitaper spectral-analysis," *IEEE Trans. Signal Process.* **40**(12), 2941–2946 (1992).
93. W. Choi et al., "Phase-sensitive swept-source optical coherence tomography imaging of the human retina with a vertical cavity surface-emitting laser light source," *Opt. Lett.* **38**(3), 338–340 (2013).
94. P. W. Wiseman et al., "Two-photon image correlation spectroscopy and image cross-correlation spectroscopy," *J. Microsc.* **200**(1), 14–25 (2000).